Jet Propulsion Laboratory
California Institute of Technology

Cassini Radio Science User's Guide

Version 1.1
2018 September 30

S. W. Asmar, R. G. French, E. A. Marouf,
P. Schinder, J. W. Armstrong, P. Tortora,
L. Iess, A. Anabtawi, A. J. Kliore, M. Parisi,
M. Zannoni, and D. Kahan

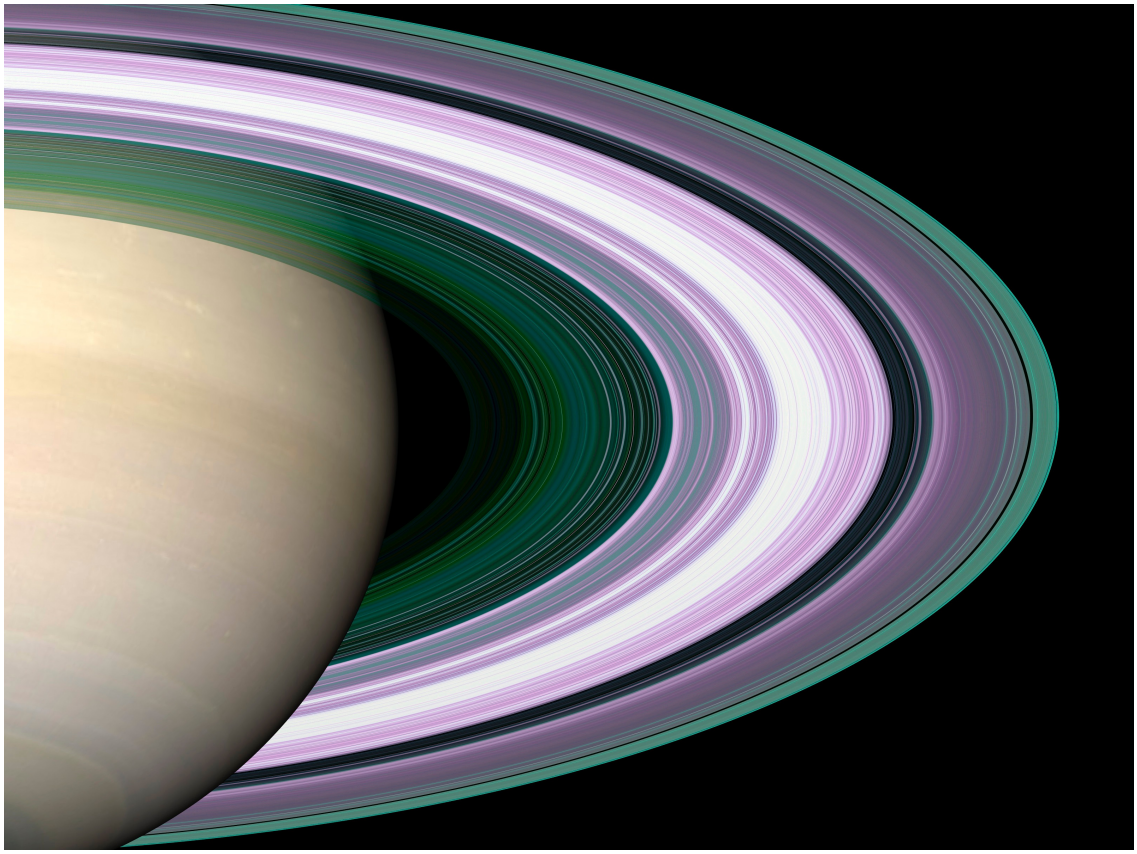

The authors acknowledge the assistance provided by the members of the Cassini Radio Science Team, JPL's Radio Science Systems Group, especially Dustin Buccino, Elias Barbinis, the Cassini-Huygens Program, and the Planetary Data System. We especially appreciate the constructive feedback from R. A. Simpson, Stanford University.

This document was prepared at the Jet Propulsion Laboratory, California Institute of Technology, under a contract with the National Aeronautics and Space Administration.

This document does not contain export-controlled information.

This document may contain references to commercial products; such references do not imply an endorsement by the United States Government or the Jet Propulsion Laboratory, California Institute of Technology.

Cover Caption: A synthesized image of the rings of Saturn derived from relative signal strength profiles from a Cassini radio occultation at 0.9, 3.6, and 13 cm wavelengths.

(CL#14-3853).

Acronyms Used in This Document

AMC	Advanced Media Calibration
ASI	Agenzia Spaziale Italiana
AACS	Attitude and Articulation Control Subsystem
ASI	Agenzia Spaziale Italiana
AU	Astronomical Unit
AWVR	Advanced Water Vapor Radiometer
bps	bits per second
BSR	Bistatic Radar
CDS	Command and Data Subsystem
CKF	C-Kernel File
COI	Center of Integration
DDOR	Delta Differential One-way Ranging
DOY	Day of Year
DSMS	Deep Space Mission Systems
DSN	Deep Space Network
EOP	Earth Orientation Parameters
ERT	Earth Received Time
ESA	European Space Agency
ET	Ephemeris Time
FFT	Fast Fourier Transform
GPS	Global Positioning System
GSE	Ground Support Equipment
GR	General Relativity
GW	Gravitational Wave
GWE	Gravitational Wave Experiment
HGA	High Gain Antenna
IAU	International Astronomical Union
IERS	International Earth Rotation and Reference Systems Service
IF	Intermediate Frequency
ION	Ionospheric calibration file
JPL	Jet Propulsion Laboratory
KAT	Ka-band Translator
kHz	kiloHertz
LCP	Left-hand Circularly Polarized
LEM	Lower Equipment Module
LGA	Low Gain Antenna
MB	Megabyte
MHz	MegaHertz
MCS	Media Calibration System
NAIF	Navigation Ancillary Information Facility
NASA	National Aeronautics and Space Administration
OD	Orbit Determination
ODF	Orbit Data File
PDS	Planetary Data System
PDT	Pointing Design Tool
PLL	Phase-Locked Loop
PMS	Propulsion Module Subsystem
PPS	Power & Pyrotechnics Subsystem
PSA	Planetary Science Archive
RCP	Right-hand Circularly Polarized
RF	Radio Frequency
RFIS	Radio Frequency Instrument Subsystem
RFS	Radio Frequency Subsystem
RMS	Root Mean Square
RS	Radio Science
RSR	Radio Science Receiver
RSS	Radio Science Subsystem
RSSG	Radio Science Systems Group
RTG	Radioisotope Thermonuclear Generator
SASF	Spacecraft Activity Sequence File
SCE	Solar Conjunction Experiment
SFDU	Standard Formatted Data Unit
SIP	Sequence Implementation Process
SIS	Software Interface Specification
SNR	Signal to Noise Ratio
SOP	Science Operation Plan
SOST	Satellites Orbiter Science Team
SP	Science Planning
SPK	Spacecraft and Planetary Kernel
SPM	Seconds Past Midnight
SPP	Science Planning Process
SSUP	Science Sequence Update Process
SVT	Sequence Virtual Team
TCB	Barycentric Coordinate Time
TCS	Temperature Control Subsystem
TDB	Barycentric Dynamical Time
TLM	Telemetry
TOST	Titan Orbiter Science Team
TNF	Tracking and Navigation File
TRO	Tropospheric calibration file
TWTA	Traveling Wave Tube Amplifier
UEM	Upper Equipment Module
ULO	Uplink Operations
USO	Ultra-Stable Oscillator
UTC	Universal Time Coordinated
VLBI	Very Long Baseline Interferometry
VSR	VLBI Science Receiver
WEA	DSN meteorological data (file)
WVR	Water Vapor Radiometer

Contents

1 Introduction and Scope

The *Cassini Radio Science User's Guide* describes data acquired during Radio Science (RS) observations of the Saturn system using the Cassini spacecraft. It also describes solar corona, relativity, and gravitational wave data collected during the Cassini-Huygens cruise to Saturn. This *User's Guide* provides an overview of the science investigations that drove the data collection and describes the types of data that resulted and how they were acquired and processed prior to delivery to the NASA Planetary Data System (PDS) for archive and use by the science community, found at
http://atmos.pds.nasa.gov/data_and_services/atmospheres_data/Cassini/rss.html.

Calibrated and diffraction-reconstructed ring occultation profiles produced by the RSS team are available at
https://pds-rings.seti.org/cassini/rss/index.html.

The rss_ringoccs open-source analysis software for ring occultation observations is hosted on Github at
https://github.com/NASA-Planetary-Science/rss_ringoccs

RS data from the Huygens descent to, and landing on, the surface of Titan are not discussed here but can be found in the European Space Agency (ESA) Planetary Science Archive (PSA) at
http://www.rssd.esa.int/index.php?project=PSA&page=huygens.

This *User's Guide* provides information that supplements documentation included with data delivered to PDS and in publications listed in the References section of this document; it is assumed that readers have access to those resources and are familiar with their contents.

2 Cassini Radio Science

The Cassini-Huygens mission to explore Saturn and its environment began with launch on October 15, 1997 and unfolded through five phases: Cruise (1997–2004), Prime Mission (2004–2008), Equinox Mission (2008–2010), Solstice Mission (2010–2016), and Grand Finale (2016-2017). Arrival at Saturn took place on 1 July 2004, the Huygens probe release took place on 25 December 2004, and the Huygens landing on the surface of Titan happened on 14 January 2005. The time following Saturn orbit insertion is known as the Saturn Tour. As will be discussed below, RS observations were carried in each of the five phases.

2.1 Radio Science Observations and Instrumentation

Radio science is the study of physical objects and phenomena using radio waves. Observables include the time, amplitude, frequency, and phase (and their dispersions) of a received signal, and its polarization. In solar system exploration, RS employs centimeter-wavelength telecommunications equipment provided on spacecraft and at ground stations. An overview of the field of and status on the recent state of the field can be found in two papers in the Decadal Study: Asmar et al., 2009a for planetary science and Asmar et al., 2009b for fundamental physics.

RS experiments are typically divided into two categories: gravitation and propagation. For gravitation, the Cassini spacecraft serves as a point-mass probe within the gravity field of Saturn and its satellites; precision measurements of the Earth-Cassini distance and relative velocity can be used to infer the target body mass and higher order field components. Propagation experiments are radio occultation experiments where the occulting objects under study are planetary ionospheres, neutral atmospheres, rings, solar plasma, cometary comae, etc.

Figure 2-1 shows typical RS observational configuration for planetary occultations. The spacecraft transmits a signal that is refracted by the target atmosphere before being received on Earth at a ground station of NASA Deep Space Network (DSN). The direction of the arrow on the dashed 'raypath' indicates that this is a 'one-way' 'downlink' observation. As the spacecraft moves, the ray probes more deeply into the atmosphere until it is absorbed or occulted by the planet itself. Stability of the signal during the observation depends on the quality of the reference oscillator onboard the spacecraft. Cassini was equipped with an Ultra-Stable Oscillator (USO) to improve stability of its transmitted one-way signal. In 'two-way' mode, a signal is transmitted from Earth and received at the spacecraft; this 'uplink' signal can then be used to control the frequency of the downlink transmission. In general, the two-way mode provides better overall frequency stability than the one-way mode because of the superior quality of the atomic clocks at the ground stations. However, passage of the uplink signal through an atmosphere, ring, or plasma cloud, or reflection from a surface distorts the uplink signal making a USO-referenced one-way mode preferable. In 'three-way' mode, one ground station transmits to the spacecraft and a different ground station receives; this is used when an observation spans the 'handover' from one ground station to another. In the Cassini case, three-way was necessary because of the long one-way light time between Saturn and Earth, ranging from 68 to 84 minutes.

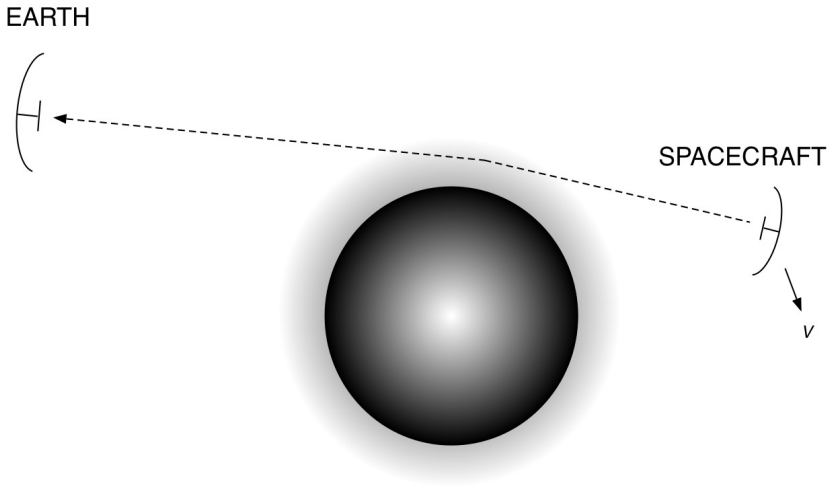

Figure 2-1: Configuration for radio science observations at a generic planet. Spacecraft moving at velocity v gets occulted by the atmosphere then the planet itself.

During occultations by Saturn, its rings, or its satellites, one-way operation yields observables which are inverted to give temperature-pressure and absorption profiles of neutral atmospheres, electron density profiles of ionospheres, and optical depth and particle size distribution profiles of rings. Most measurements are wavelength dependent and some may include polarization effects, so a wide range of transmitting and receiving equipment is desirable.

During close encounters, the spacecraft antenna is rotated from the Earth direction to point at satellite surfaces or Saturn's ring plane. Such one-way bistatic radar (BSR) experiments require the highest sampling rates of the receivers at the ground stations and contain the most interesting polarization information. Inversions can yield dielectric constant of target surfaces and size distributions for ring particles.

2.1.1 **Cruise Phase Science**

During the long Cassini cruise phase, RS observations included Gravitational Wave Experiments (GWEs) near solar oppositions and Solar Conjunction Experiments (SCEs). In a GWE, subtle changes in the apparent Earth-spacecraft distance and/or relative velocity, which cannot be attributed to other causes, would indicate passage of gravitational wavefronts through space between Earth and Cassini. GWE observations were conducted in two-way mode for highest frequency and timing stability. When the spacecraft's radio signal is occulted by the Sun, a SCE investigates the solar corona. Operationally, two-way data are collected at large solar radii, but one-way operation with open-loop reception (described below) is the practical choice for small solar radii and high solar activity. The shortest radio wavelengths are least affected by the solar plasma; multiple wavelength measurements yield total electron content along the radio path directly.

2.2 Spacecraft

The Cassini spacecraft was comprised of four primary modules: the high-gain antenna (HGA), two equipment modules, and the propulsion module. These contained a number of spacecraft subsystems, including twelve science instruments. Three Radioisotope Thermoeletric Generators (RTGs) were mounted in the equipment modules; an external boom for the magnetometer was attached to the Upper Equipment Module (UEM). The most relevant subsystems for RS are discussed below.

2.2.1 Radio Frequency Subsystem

The Radio Frequency Subsystem (RFS), in conjunction with the Antenna Subsystem, provided communications between the spacecraft and ground stations of the DSN. It also provided a signal source for RS measurements. In earlier documentation (*e.g.*, Kliore *et al.,* 2004) a distinction was made between multi-use radio components (RFS) and RS-only components called the Radio Frequency Instrument Subsystem (RFIS) but that distinction is not maintained here, and all radio components fall within the RFS. The RFS included a pair of redundant X-band transponders for reception and transmission, an S-band transmitter, and a Ka-band transmitter. The USO provided an onboard highly stable time and frequency reference, but it failed in 2011. A Ka-band translator (KaT), which received at 34 GHz and transmitted coherently at 32 GHz, supported general relativity observations during Cruise; it failed before Saturn orbit insertion.

The RFS produced an X-band carrier modulated with data received from the command and data subsystem (CDS), amplified the modulated carrier, and delivered the signal stream to the Antenna Subsystem for transmission to Earth. It also received and demodulated X-band commands from the ground via the Antenna Subsystem. At Saturn, where the one-way distance to Earth is 8.2-10.2 astronomical units (AU) and the one-way travel time is 68-84 minutes, commands and instructions from Earth were received at 1000 bits per second (bps) by the HGA; and data were transmitted to Earth at selectable rates ranging from 14,220 to 165,900 bps. Data could be recorded on the solid-state recorders for about 15 hours, while the HGA was not pointed at Earth; then they are played back for nine hours. About one gigabit of data could be returned each day via a 34-m DSN antenna; nearly four times that can be returned via a 70-m ground antenna. The two redundant recorders could record and read out nearly 2 gigabits of data simultaneously. The CDS handled combined data rates in excess of 430,000 bps from the instruments while carrying on its functions of command and control. Since RS observables are generated at the DSN, only a very small fraction of telemetry, such as equipment status and spacecraft attitude measurements, are of interest to RS.

The Antenna Subsystem included the 4-meter diameter HGA reflector (which was also used for Sun shading in the early cruise phase); a frequency-selective sub-reflector; HGA feeds for S-, X-, Ka-, and Ku-bands; and two low-gain antennas (LGA). All antennas operated at X-band; only the HGA operates at S-, X-, Ka-, and Ku-bands. The X-band components are for communications and navigation as well as RS; the S- and Ka-band

components are only for RS, and the Ku-band components are for the Cassini RADAR. Table 1-1 lists the RS bands.

Table 1-1: Cassini Radio Science Bands and Wavelengths.

Band	Wavelength (cm)	Frequency (MHz) Uplink	Frequency (MHz) Uplink
S	13	N/A	2298
X	3.6	7175	8425
Ka	0.9	34316	32028

Notes: Separate S-band channels existed to receive the Huygens probe relay in two polarizations at 2040 and 2098 MHz. The X-band uplink polarization is left circular (LCP) when Transponder A is selected and right circular (RCP) when Transponder B is selected. The X-band downlink polarization is LCP when traveling wave tube amplifier A (TWTA-A) is selected and RCP when TWTA-B is selected.

2.2.1.1 **USO**

Key to RS instrumentation onboard the Cassini spacecraft, the USO provided the highly stable reference generated on-board the spacecraft until it failed in 2011. The Cassini oscillator was in the class of highest performance thermally-controlled quartz crystal oscillators flown on planetary missions. It was manufactured by Johns Hopkins University, Applies Physics Laboratory. Figure 2-2 shows the X-band output frequency of the USO over several years showing long-term aging behavior (without accounting for time dilation effects).

Figure 2-3 shows the excellent Allan Deviation performance of the USO stability as a function of integration time from one representative test in 2011. These data in reality characterize the end-to-end performance of the radio systems on both the spacecraft and ground station, although independent calibration of the DSN stations have shown that these results are dominated primarily by the limit of the USO performance.

2.2.2 **Attitude and Articulation Control Subsystem**

The Attitude and Articulation Control Subsystem (AACS) maintained the spacecraft's orientation and consists of redundant Sun sensors mounted on the HGA, redundant stellar reference units mounted on the remote-sensing platform, three mutually perpendicular reaction wheels mounted in the Lower Equipment Module (LEM), plus a fourth backup reaction wheel mounted in the UEM. Redundant inertial reference units, along with an accelerometer to measure changes in the spacecraft's velocity, are located in the UEM.

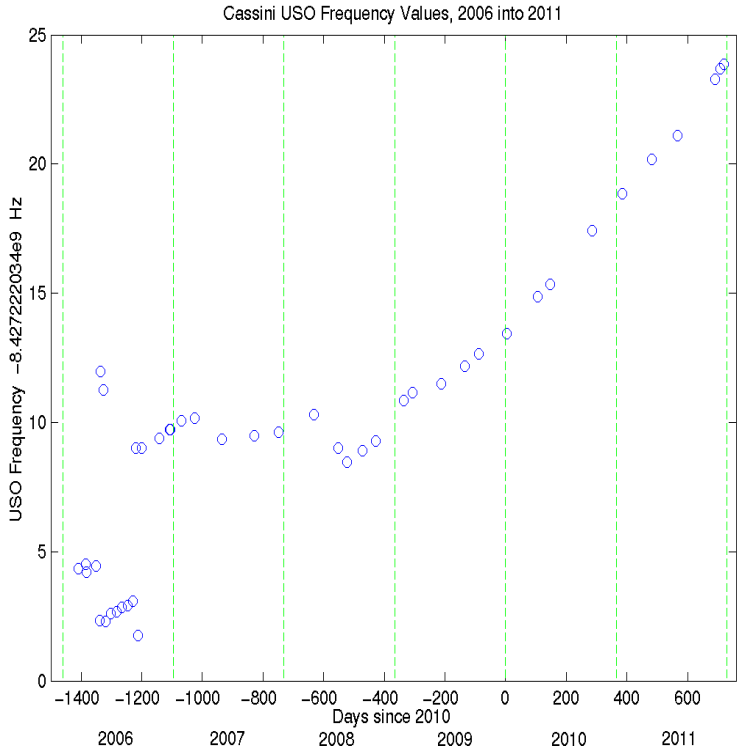

Figure 2-2: The USO output frequency scaled to X-band by the Cassini transponder over several years, showing long-term aging process as expected.

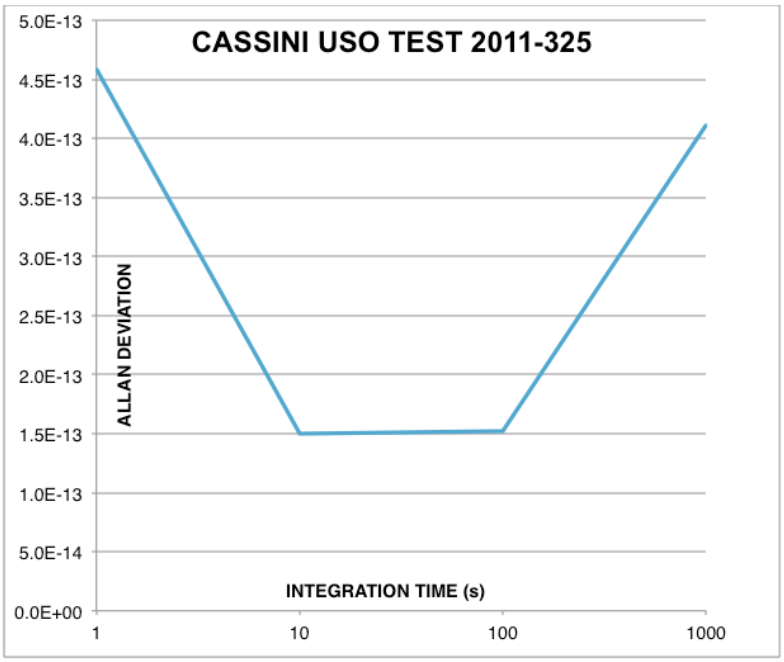

Figure 2-3: Allan Deviation of the Cassini USO as a function of integration time from a representative test. Four points are plotted at 1, 10, 100, and 1000 seconds.

The AACS points the selected communication antenna toward Earth and points the remote sensing pallet toward selected targets. It also points one of the two redundant main propulsion engines in the desired direction during engine burns and performs small trajectory correction maneuvers using the onboard thrusters. The AACS uses a pointing system known as inertial vector propagation that keeps track of spacecraft orientation, the direction of the Sun and distance to the Sun, Earth, Saturn, and other possible remote-sensing targets, and the spacecraft-relative pointing directions of all science instruments. This subsystem provides sufficient engineering data to support science data interpretation and mission operations.

2.2.3 **Other Subsystems**

The Propulsion Module Subsystem (PMS) is the largest and most massive subsystem. It consists of a bipropellant element for trajectory changes and a hydrazine element for attitude control, small maneuvers, and reaction wheel desaturation. The Power and Pyro-technics Subsystem (PPS) converts the RTG power output to provide a regulated 30-V direct-current power bus and provides the capability to turn various users on or off when commanded. Power conditioning equipment can detect over-current conditions and switch the affected user off. The pyrotechnic switching unit also provides redundant power conditioning and energy storage, and it controls the firing of pyrotechnic devices.

The Temperature Control Subsystem (TCS) maintains the temperatures of all critical spacecraft components within their specified limits via electrical temperature sensors. Even at 9 AU from the Sun, spacecraft orientations that expose radiator plates to the Sun can severely degrade the data collected by some of the science instruments. The TCS can turn electric heaters on or off, open or shut thermal louvers in the UEM, use small radioisotope heaters to raise the temperature of selected regions, and utilize thermal blankets and shields. Several instruments have radiator plates for cooling.

2.3 **Ground Systems**

RS data are acquired by the ground instrumentation at DSN stations at Goldstone, California; Canberra, Australia; and Madrid, Spain. (During the F ring and proximal orbits, additional European Space Agency (ESA) ground stations were employed as well.) The microwave signals are captured using 34- or 70-m diameter antennas and are mixed to lower frequencies where they are sampled, averaged, and recorded for later analysis. Two- and three-way uplink transmissions can be modulated with ranging codes, which allow determination of round-trip times after correlation with the modulation on the downlink signal. Status and performance of the uplink, downlink, and ground antenna systems is recorded in files of 'monitor' data. RS data are acquired via two types of receivers, closed- and open-loop.

The ground stations are pointed via the following techniques. Conical scan is dynamical ground antenna pointing during which the boresight is offset from the predicted pointing by a small amount; the observed degradation in signal level is used to determine a new best pointing direction. This is repeated in such a way that the pointing follows a conical path

around the best direction; it is not used when the signal is expected to undergo significant amplitude changes. The monopulse technique uses relative amplitude and phase between TE_{11} and TE_{21} circular waveguide mode signals generated in a special Ka-band feed. Aberration correction is a pointing adjustment to account for real motion of the signal source against the sky background during the one-way light travel time. During uplink, the antenna is pointed to the location where the spacecraft will be at the time the signal arrives rather than toward its geometric location at the time of transmission.

2.3.1 **Closed-Loop Tracking Receiver**

In order to track a spacecraft signal carrier, the closed-loop receiver utilizes a phase-locked loop (PLL) that precisely measures and record the carrier's phase. The Doppler shift is estimated from the phase and converted to relative velocity. Separately, ranging code modulation is extracted and correlated with the uplink code to determine absolute range. The closed-loop tracking receiver provides a Doppler estimate every 0.1 seconds; ranging samples are generated at a rate that depends on the code repetition period and user-selected averaging interval. The tracking receiver also provides a signal to the antenna pointing process.

2.3.2 **Open-Loop Radio Science Receiver**

In open-loop reception, an independent broad band receiver is used without the phase-lock loop tracking mechanism described above. The Radio Science Receiver (RSR) down-converts the spacecraft signal via a local oscillator heterodyne process guided by a prediction of the expected frequency. Additional description of the RSR structure and data format and content is available in the DSN document 820-013, 0159-Science; a functional description in Asmar et al., 2013. It captures and records the pre-detection radio signal at a user-selected sampling rate via an analog-to-digital converter. The digital samples of the propagating electromagnetic wave are stored to disk. Because the received downlink signal can be precisely reconstructed, this mode of data acquisition provides great flexibility in signal processing. The RSR provides superior phase stability, captures the signal during high amplitude or frequency dynamics (where the closed-loop receiver would lose lock), is resilient to multi-path effects, and preserves all the information contained in the signal. On the other hand, this method requires additional operational procedures, resources, and generation of predictions sometimes containing complex planetary atmospheric or other models It also involves handling large file sizes and requires expertise in digital signal processing.

Each DSN complex has at least three RSRs, each capable of independently capturing the output from a different antenna feed; i.e., a different band polarization combination. Similar receivers (VSRs) are also available for VLBI work; their output can be easily converted to the RSR format, and they can be used when Cassini RS observations require more support than the RSRs alone can provide. The Radio Science Systems Group (RSSG) remotely operates the RSRs and VSRs from JPL.

2.3.2.1 **Radio Science Receiver Observables and Analysis**

2.3.2.1.1 **Data Samples and RSR Output Frequency**

As described in the 820-013 document, the spacecraft transmits a signal at S-Band, X-Band, or Ka-band, to a station where the received the Radio Frequency (RF) signal is down converted to an Intermediate Frequency (IF) signal of about 300 MHz and then fed via a distribution network into an RSR. The signal is then digitized and passes through a digital down converter whose function is to select a 16 MHz channel through the use of Finite Impulse Response filters with revolving banks of filter coefficients. The data stream is separated into eight decimated data streams that are fed into two sets of filters, one set produces In-phase (I) data while the other produces Quadrature-phase (Q) data. Each of the complex samples contains 8-bit, or I and Q components. The size of the output samples is adjustable: 1, 2, 4, 8, and 16-bit samples are supported. The reduction in sample size is accomplished through truncation.

The first analysis step is to unpack the samples to get I/Q pairs as a function of time. From these data the signal frequency can be computed from the RSR output by, for example, a software phase-lock loop or non-coherently using a fast Fourier transform (FFT) method.

2.3.2.1.2 **Sky Frequency**

The RSR-level frequency can be converted to downlink sky frequency using the tuning information included in the RSR data files. Briefly: the RSR files include two numbers which are valid for the whole data file, the radio-frequency-to-intermediate frequency factor used by the station (RF-to-IF) and the digital down converter local oscillator (DDC-LO). For each second of RSR data, the files also contain 3 frequency-tuning polynomials (p1, p2, p3):

$$sky_{freq}(t) = RF\text{-}to\text{-}IF*10^6 + DDC\text{-}LO*10^6 - dp_{nco} + RSR(t) \quad (1)$$

where sky_{freq} is in Hz, RSR(t) is the signal frequency in the RSR output (Hz), and

$$dp_{nco}(t) = p1 + p2*(n_{msec}/1000) + p3*((n_{msec}/1000)^2)) \quad (2)$$

where "n_{msec}" is the number of milliseconds within each second's worth of tuning polynomials. Computation must be done in double or quad precision to ensure sufficient accuracy in the results.

2.4 **Observation Planning**

A sequence is an approved list of time-ordered spacecraft activities sent to the spacecraft on a periodic basis. Creating a sequence is a multi-step process involving a number of Cassini teams over many weeks. Sequences are usually built around one or more key events planned for each Cassini orbit.

Of critical importance to Cassini RS are the spacecraft trajectory and attitude prediction and the quality of the reconstruction. For Cruise, the Cassini HGA was simply pointed continually toward Earth and neither GWE nor SCE required maneuvers or attitude changes. During the Saturn Tour, some RS observations had tight timing and pointing requirements that could only be met if the designs were updated a few days before the observation execution. Shortly before these observations, such as atmospheric occultation and Titan bistatic observations, the Navigation Team delivered a special Orbit Determination (OD) solution and other products to allow the RS Team to assess the impact of trajectory changes and uncertainties on the observations. If needed, timing and/or pointing changes could be made and uplinked to the spacecraft. In order for future users of archived Cassini data to better understand the final products resulting from the science planning process at various mission phases, it is useful to know the time evolution of observation planning and implementation.

The Cassini primary mission was organized into teams that conduct the Science Planning Process (SPP) for scientific observations into integrated and conflict-free timelines of the spacecraft's orbit around the Saturn system, referred to as 'revs.' These teams were the Titan Orbiter Science Team (TOST), the Satellites Orbiter Science Team (SOST), and the Rings, Saturn, and Cross-Disciplinary Target Working Teams (TWTs). Science working groups on surfaces, atmospheres, rings, and magnetospheres also worked to resolve conflicts that could not be resolved in those teams. This happened for science planning that consists of production of a Science Operation Plan (SOP) that lead to the generation of a sequence of commands to be sent to the spacecraft. A Sequence Virtual Team (SVT) was responsible for integrating a conflict-free sequence to the command level.

A five-week updates process, known as the aftermarket, was applied to the SOP due to adding science observations, implementation liens, performance changes, or recent scientific discoveries. Negotiations and changes that involve multiple tour segments were treated in a joint meeting of all the involved TWTs and OSTs. The SOP was then updated to reflect changes with attention to actual DSN station allocations and new ephemeris files. A final step before uplink is called the Science and Sequence Update Process (SSUP) and was started approximately 10 weeks before the sequence start date, with ongoing attention to revisions in pointing and DSN allocations. The SOP development produced Spacecraft Activity Sequence Files (SASF) containing Pointing Design Tool (PDT) designs, operations mode transitions, telemetry modes and more.

For the Cassini Equinox Mission, the process was simplified into just-in-time products such as handoff packages, checklists, and DSN requests that were delivered 2 weeks prior to SOP with no aftermarket. The SOP was a 14-week process, followed by a 10-week SSUP similar to prime mission. Sequence execution was 5 weeks, with 6 overlapping processes taking place at a time. In the Solstice mission, the process was further simplified to allow integration of the tour with significantly less workforce. Implementation was changed to one process called Sequence Implementation Process (SIP) which process was divided into five 'ports.' Port 1 began with the integration handoff products. The next two ports began with the end products from the previous ports. The remaining ports completed with a safe

flyable sequence. The sequence development lasted 22 weeks (compared to 24 during the Equinox mission), and sequence execution was 10 weeks (compared to 5 weeks in the Equinox mission), with 3 overlapping processes at a time.

The Cassini RS team participated in mission planning by initially proposing specific observations and following up the process throughout its various stages. The configuration of which of the three possible frequency bands (S, X, or Ka-bands) would be utilized is called an operations mode or opmode is negotiated during this process considering power limitations on-board the spacecraft. During the life of the mission, due to the normal spacecraft power reduction, other instruments, selected through negotiations, had to be powered off or go to sleep mode to save the power needed to allow RS to use certain opmodes. Some RS observations, such as atmospheric occultation and Titan bistatic observations had tight timing and pointing requirements that could only be met if the designs were updated a few days before the observation execution. Shortly before these observations, the Navigation team delivered a special Orbit Determination (OD) solution and other products to allow the RS team to assess the impact of trajectory changes and uncertainty on the observations. If needed, timing and/or pointing changes were made and uplinked to the spacecraft.

2.5 Data Archives

For each RS experiment, the following types of files are available through the Planetary Data System. Where documents have been cited, dates are not given because each document has evolved and several versions may have been used during the course of the Cassini mission. An appropriate version should be included in the DOCUMENT directory of each Cassini archival data set.

2.5.1 Science Observable Files

Files with science observables include closed-loop Doppler (and sometimes range) as well as open-loop RSR recordings. These are the fundamental measurements for each Cassini RS investigation. Two sets of fundamental observables and a set of ancillary data files are described below.

2.5.1.1 Tracking and Navigation File (TNF)

Each closed-loop receiver generates a data file called a Tracking and Navigation File (TNF). Data accumulate at a rate of about 3 Megabytes (MB) per hour per closed-loop receiver. A typical TNF contains Doppler phase measurements, Delta Differential One-way Range (DDOR) values, and selected ground system status information. The TNF is the most primitive output from the closed-loop system. Phase measurements are the highest quality tracking data available to spacecraft navigators and gravity investigators. Differencing phase measurements yields the more traditional line-of-sight Doppler values. Figure 2-4 shows representative contents of a TNF file. The format is described by the TRK-2-34 document:

820-013, Deep Space Mission System (DSMS) External Interface Specification
JPL D-16765

TRK-2-34: DSMS Tracking System Data Archival Format

2.5.1.2 **Orbit Data File (ODF)**

Orbit Data File (ODF) is an abstracted version of the TNF. It has been the fundamental input to orbit determination processes for decades, and its format has remained very stable over that time. Its primary content is line-of-sight Doppler and range, rather than phase. Like the TNF, a single ODF usually represents the output from the closed-loop tracking system following a single spacecraft over one or more DSN tracking sessions or 'passes.' The data accumulation rate is a selectable parameter. A rate of 130 kilobytes (kB) per hour is typical for single frequency tracking at 1 second sampling. The ODF format is described by the TRK-2-18 document:

820-013, Deep Space Mission System (DSMS) External Interface Specification
JPL D-16765
TRK-2-18: Tracking System Interfaces: Orbit Data File Interface

2.5.1.3 **Radio Science Receiver Data (RSR)**

Open-loop data are captured in the Radio Science Receiver (RSR) Standard Formatted Data Unit (SFDU). RSR output samples at a single rate (up to four channels at different sampling rates can be captured by a single RSR) are stored in records with housekeeping data from the RSR (such as phase and frequency of the programmable oscillator). Sample resolution and rate can vary from 16 bits at 1 kHz to 1 bit at 16 MHz. Each RSR can capture data from a different band and polarization pair. RSR file content and format are described by the 0159-Science document:

820-013, Deep Space Mission System (DSMS) External Interface Specification
JPL D-16765
0159-Science: Radio Science Receiver Standard Formatted Data Unit (SFDU)

2.5.2 **Calibration and Ancillary Information**

Measured observables require proper calibrations to correct for deterministic error sources. Various calibration files are provided by the DSN for the ground-based elements of the RS instrumentation and by the flight project for the spacecraft elements.

2.5.2.1 **Earth Orientation Parameters (EOP)**

Data in the DSN Earth Orientation Parameters (EOP) file describe the motion of the Earth in inertial space in terms of the orientation of its rotation axis and the angle through which the Earth has rotated on its spin axis since some reference epoch. The EOP file is used to calculate the Doppler contribution to a measurement from Earth rotation. The file and its contents are described by the TRK-2-21 document:

820-013, Deep Space Mission System (DSMS) External Interface Specification

TRK-2-21: DSN Tracking System Earth Orientation Parameter Data Interface

```
          Report for File: S82TIGF2014_065_0110XMMMV1.TNF
          Generation Date: 2014-246T20:50:42
               Start Time: 2014-065T01:10:53
                 End Time: 2014-066T06:25:00
            Spacecraft ID: 82
          Downlink DSS ID: 25, 34, 55
           Downlink Bands: X, Ka
            Uplink DSS ID: 25, 34, 55
             Uplink Bands: X
            Tracking Mode: None, 2W, 3W/34, 1W, 3W/25, 3W/55
       Number of Records: 960566
    Available Data Types: 0, 1, 2, 3, 7, 9, 11, 16, 17
                         00: Uplink Carrier Phase - 145102
                         01: Downlink Carrier Phase - 235504
                         02: Uplink Sequential Ranging Phase - 108016
                         03: Downlink Sequential Ranging Phase - 258
                         07: Sequential Ranging - 258
                         09: Ramps - 236
                         11: DRVID - 258
                         16: Carrier Observable - 235467
                         17: Total Phase Observable - 235467

DSS-25 X-band Downlink:
                      3W/55 @ 2014-065T07:37:09 - 2014-065T10:42:32
                         2W @ 2014-065T10:42:33 - 2014-065T15:17:37
                      3W/34 @ 2014-065T15:17:38 - 2014-065T16:55:57
DSS-25 Ka-band Downlink:
                      3W/55 @ 2014-065T07:37:45 - 2014-065T10:42:32
                         2W @ 2014-065T10:42:33 - 2014-065T15:17:37
                      3W/34 @ 2014-065T15:17:38 - 2014-065T16:56:02
DSS-34 X-band Downlink:
                      3W/25 @ 2014-065T12:30:04 - 2014-065T15:17:30
                         2W @ 2014-065T15:17:31 - 2014-066T00:46:56
DSS-34 Ka-band Downlink:
                      3W/25 @ 2014-065T12:30:04 - 2014-065T15:17:30
                         2W @ 2014-065T15:17:31 - 2014-066T00:47:02
DSS-55 X-band Downlink:
                         1W @ 2014-065T03:40:37 - 2014-065T05:28:21
                         2W @ 2014-065T05:29:36 - 2014-065T09:06:16
                      3W/34 @ 2014-066T00:20:04 - 2014-066T03:03:36
                         1W @ 2014-066T03:03:50 - 2014-066T03:23:04
                         2W @ 2014-066T03:24:22 - 2014-066T05:47:05
DSS-55 Ka-band Downlink:
                         1W @ 2014-065T03:45:50 - 2014-065T05:28:21
                         2W @ 2014-065T05:29:36 - 2014-065T09:06:20
                      3W/34 @ 2014-066T00:20:04 - 2014-066T03:03:35
                         1W @ 2014-066T03:03:48 - 2014-066T03:23:04
                         2W @ 2014-066T03:24:22 - 2014-066T05:46:22
```

Figure 2-4: An example of the contents of a Tracking and Navigation File

2.5.2.2 **Media Calibration Data (TRO and ION)**

Tropospheric (TRO) files and ionospheric (ION) files contain estimates of the radio delay in the Earth's troposphere and ionosphere, respectively, for use in calibrating their effects on the measured phase of the uplink and downlink carrier signals. These files are described by the TRK-2-23 document:

820-013, Deep Space Mission System (DSMS) External Interface Specification
JPL-16765
TRK-2-23: Media Calibration Interface

2.5.2.3 **Advanced Water Vapor Radiometer (WVR/AWVR) Data**

The fixed Water Vapor Radiometers (WVR) measure the water emission in the atmosphere. At selected DSN stations, an advanced version (AWVR) measures emissions at 20.7 and 31.4 GHz along the line of sight to the spacecraft being tracked. The WVR is part of DSN operations; the AWVR is remotely operated for the DSN by the RSSG from Pasadena. It is an element of a bigger Advanced Media Calibration (AMC) system. The data files are described by:

Cassini Document DORS-002
Software Interface Specification
Media Calibration System (MCS) Path Delay File

2.5.2.4 **DSN Monitor Data**

The DSN generates a real-time stream of status and performance data from its own systems 'monitor' data; the data may be used for anomaly resolution, performance validation, and calibration of other data. Some Cassini RSS data sets include edited versions of this stream. Parameters may include azimuth and elevation angles of the antenna, monopulse correction values, carrier frequency, wind speed and direction, lock status of the closed-loop PLL, receiver system noise temperature, and carrier signal-to-noise ratio. The data are stored in ASCII tables with labels, which describe both the format and content.

2.5.2.5 **Spacecraft Engineering Telemetry (TLM)**

The spacecraft also generates a real-time stream of status and performance data from onboard systems, which can be downlinked in parallel with or separately from science data. These data may be used for anomaly resolution, performance validation, and calibration of other data. Parameters of interest to RS include lock status of spacecraft receivers, power output of spacecraft transmitters, and physical temperatures at various points on or within the spacecraft. Some Cassini data sets include edited versions of this data stream. Files are ASCII tables, which are accompanied by labels describing both the format and content of the tables.

2.5.2.6 **Spacecraft and Planetary Kernel (SPK)**

The Navigation Team provides a reconstructed the spacecraft trajectory after spacecraft maneuvers. The ephemerides of Earth, Saturn, and its moons are included and allow Doppler calibration of the RS data. The SPK file is described by:

Spacecraft and Planetary Ephemeris Kernel
NAIF Document No. 367
Navigation and Ancillary Information Facility (NAIF)
Jet Propulsion Laboratory, Pasadena, CA

2.5.3.7 **C-Kernel (CKF)**

The navigation team provides a file of reconstructed spacecraft orientation in inertial. It is available as a NAIF C-Kernel in order to determine HGA pointing, described by:

SPICE C-Matrix Kernel
NAIF Document No. 370
Navigation and Ancillary Information Facility (NAIF)
Jet Propulsion Laboratory, Pasadena, CA

3 Radio Science Investigations

In the previous section, an overview of the RS observations obtained using Cassini and the raw data types preserved in the Cassini RSS archive were presented. In this section, a detailed explanation is presented of how the science analysis proceeds for each investigation, leading to higher-level data products.

3.1 Gravity

Traditional estimates of the physical properties of planetary bodies - their masses, sizes, shapes, and orbits - were based on remote optical observations. The ability to make direct and precise distance and velocity (range and range-rate) measurements of spacecraft under the influence of a target body's gravitational field revolutionized this area of solar system exploration.

The application of RS techniques to celestial mechanics began with the 1962 Mariner 2 mission to Venus and the 1962 Ranger mission to the Moon. Using the ground station-generated Doppler data from Mariner 2, Anderson and Warner (1966) were able to make order-of-magnitude improvements over the previous Earthbound determinations of the masses of the Moon and Venus. With the Ranger mission, estimates were made of the masses of the Moon and Earth and an estimate was made of the offset between the lunar center of gravity and center of figure. Subsequently, Mariner 4 (Mars), Mariner 5 (Venus), and Mariner 9 (Mars) provided the mass and first estimates of low order gravitational harmonics for Venus and Mars (Anderson, 1974), while analysis of Doppler measurements from the Lunar Orbiter and Apollo missions led to the discovery of large positive gravity anomalies (mascons, or mass concentrations) on the Moon (Muller and Sjogren, 1968).

The mean density of a planet is determined from its bulk volume and mass, which is obtained by measurement of the gravity. Volume is derived from a shape model based on images, topographic altimetry, and/or radio occultations. Information about the internal structure of the body, when combined with an optical or radar map of surface features, can constrain models describing the differentiation of interior layers and the chemical composition and physical state of the interior. In turn, these models can be used in arguments for different theories of solar system evolution.

Gravity RS has developed rapidly and has been utilized to some extent in every planetary mission. The Cassini spacecraft has been used to study Saturn and its gravity field, which has been determined using RS measurements to 2nd degree and order so far (Iess et al., 2010). As Cassini loops through Saturn's system, it has flown by several large moons; gravity measurements have been carried out at Titan, Enceladus, Rhea, and Dione. Their masses and mean densities have been characterized, and deductions have been made about their interior properties (Kliore et al., 2004, Iess et al., 2010, Iess et al., 2012).

Precise radio tracking of Cassini at Titan has provided a determination of Titan's mass and gravity harmonics to degree and order 3. Titan's quadrupole field is consistent with a hydrostatically relaxed body, shaped by tidal and rotational forces. The inferred moment of inertia is about 0.34, implying incomplete differentiation either in the sense of imperfect separation of rock from ice or a core in which a large amount of water remains chemically bound in silicates. The equilibrium figure is a triaxial ellipsoid whose semi-axes a, b, and c differ by 410 meters (a – c) and 103 meters (b – c). Non-hydrostatic geoid height variations of up to 19 meters are small compared to the observed topographic anomalies of hundreds of meters, suggesting a high degree of compensation appropriate to a body that has warm ice at depth, (Iess et al., 2012).

3.1.1 **Gravity Field Representation**

The gravitational field is typically represented by an nth degree and order spherical harmonic series expansion. The gravitational constant for the body *GM* scales the harmonics of the field. Additional lower degree terms describe the dynamic flattening and the orientation of the principal rotational axes while placing constraints on the deep interior structure. Higher degree terms describe, in increasing detail, smaller and shallower local gravity features on or near the surface, including mountains and craters. This representation follows the solution to Laplace's equation for the gravitational potential, *U,* is for a sphere. The solution with normalized coefficients ($\bar{C}_{nm}, \bar{S}_{nm}$) is expressed as (Kaula, 1966):

$$U = \frac{GM}{r} + \frac{GM}{r}\sum_{n=2}^{\infty}\sum_{m=0}^{n}\left(\frac{R_e}{r}\right)^n \bar{P}_{nm}(\sin\phi_{lat})\left[\bar{C}_{nm}\cos(m\lambda) + \bar{S}_{nm}\sin(m\lambda)\right] \tag{1}$$

where G is the universal gravitational constant (6.67384 10^{-11} N(m/kg)^2), M is the target body mass, n is the degree, m is the order, $\bar{P}_{nm}$ are the fully normalized associated Legendre functions, R_e is the reference radius of the sphere, ϕ_{lat} is the latitude, and λ is the longitude

(positive east). The gravity coefficients are normalized and are related to the un-normalized coefficients by (Kaula, 1966):

$$\begin{pmatrix} C_{nm} \\ S_{nm} \end{pmatrix} = \left[\frac{(n-m)!(2n+1)(2-\delta_{0m})}{(n+m)!} \right]^{1/2} \begin{pmatrix} \bar{C}_{nm} \\ \bar{S}_{nm} \end{pmatrix} \tag{2}$$

where δ is the Kronecker delta. The coefficients contain the information about the variation of gravity, and n and m describe the resolution of the field that can be translated to surface resolution.

3.1.2 **Data Processing**

The procedures for deriving gravity field models are closely linked to the problem of Orbit Determination (OD) for interplanetary spacecraft. The OD process is an iterative estimation based on the comparison between measured observables and the corresponding observable values computed from mathematical models described in Moyer (2003). The differences between the observed and modeled observables are residuals. The goal of the OD process is to estimate of a set of parameters ('solve-for' parameters) that unambiguously define the spacecraft trajectory and the corresponding covariance matrix that defines the formal uncertainty of the solution. These estimated parameters minimize the residuals in a least square sense.

For mission navigation, the OD software tools are designed to analyze large data sets and extract values for a large number of solve-for parameters with the aim of providing the best estimate of spacecraft state, the time-dependent inertial position and velocity. RS typically has small data sets acquired during the limited time intervals of dedicated observations. These are analyzed to estimate the spacecraft state and a restricted set of parameters that define the gravity field. These measurement procedures are carefully designed to minimize the uncertainties in the OD process and to maximize the signal-to-noise ratio of the solve-for parameters.

For Cassini gravity investigations, the solve-for parameters include *GM* and the coefficients that define the spherical harmonics expansion of the gravitational field, the Love numbers that define the gravity field response to external tidal forces, and the target's rotational parameters. The OD process can be divided into four steps:

1. Pre-processing of measured observables
2. Calculation of computed observables and partial derivatives as well as residuals with respect to the solve-for parameters
3. Application of an estimation filter
4. Solution analysis

The solution is intrinsically non-linear. In the first iteration, the observables and partials are computed using *a priori* values of the solve-for parameters. The estimation filter then

computes differential corrections to these values; the calculation step is repeated with updated values until some level of convergence is reached (see Figure 3-1). The steps are described below from an operational point of view.

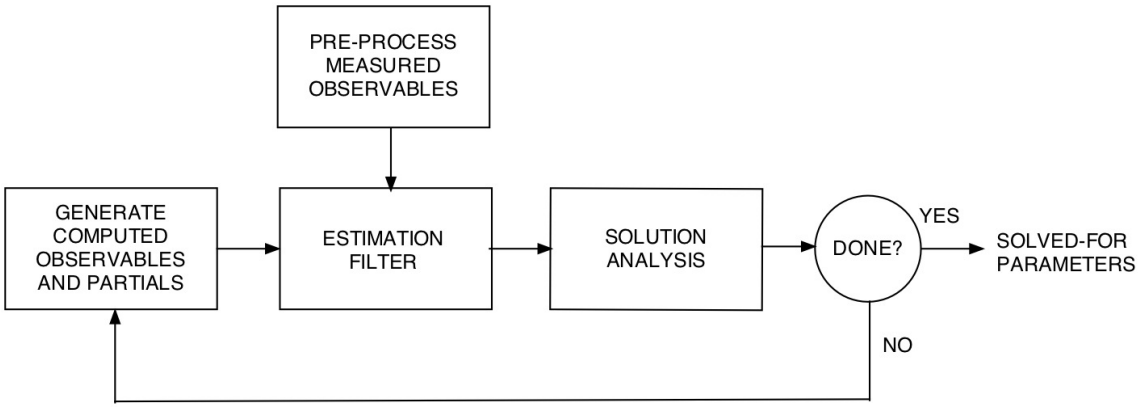

Figure 3-1. Flow diagram for gravity solution.

3.1.2.1 **Pre-processing of Radiometric Measurements**

The primary observables are (Sections 2.5.1.1 and/or 2.5.1.2):

- Range: measured round-trip light time, or distance, in range units.
- Doppler: measured frequency shift of the carrier of the received signal due to relative transmitter-receiver motion.
- DDOR: the measured angular position of the spacecraft in the plane of the sky along a baseline formed by two ground stations.

One or more of the following actions may be performed before the OD analysis:

- Apply calibrations to observables to correct for group delay due to ground and spacecraft electronics and group and phase delay due to the troposphere, ionosphere, and interplanetary plasma (section 2.5.2.2).
- Compute received sky frequencies from open-loop recordings (section 2.3.2.1.2) when available.
- Compute synthetic non-dispersive observables using a multi-frequency link (section 2.1).
- Delete outliers; typically as many as 20% of the measured observable values are removed in this step.

3.1.2.2 **Calculation of Observables and Partials**

During the calculation step, observables are computed using mathematical models of all non-negligible physical effects. The mathematical models depend upon the numerical values of three types of parameters:

- ***Solve-for parameters*** are imperfectly known parameters that affect the data and whose current estimate can be improved through the OD process. The solve-for parameters are a set of model parameters for which the estimation filter computes a differential correction of their central values along with their uncertainties, in the form of a covariance matrix. The latter is obtained by inverting the information matrix. The information matrix is built from the partial derivatives of the observables with respect to the solve-for parameters along with the residuals. For the first iteration, solve-for parameter *a priori* values and uncertainties are obtained from the best measurements or theoretical estimations available to date. In subsequent iterations, the solution obtained at the previous iteration is used. The solve-for parameters should always include the initial position and velocity of the spacecraft.
- ***Consider parameters*** are not-exact parameters that affect the data and whose current estimate cannot be improved through the OD process. Their best estimates to date must be used in the mathematical models, together with their uncertainties. The uncertainties of consider parameters increase the overall solution uncertainty but do not change the estimates for the solve-for parameters.
- ***Exact parameters*** have uncertainties that do not affect the estimation because they are negligible with respect to their influence on observables.

During the calculation step, partial derivatives of the observables with respect to the solve-for and consider parameters are computed. The partials are used to obtain the new estimates of the values of the solve-for parameters and their covariance matrices.

3.1.2.2.1 Planetary and/or Satellite Ephemeris Update

During the calculation step, it may be necessary to update planetary and/or satellite ephemerides. For example, during gravity observations of a Saturnian satellite, the Cassini trajectory is affected in a non-negligible way by the gravitational fields of both Saturn and the satellite. The measured observables are sensitive to the relative positions and velocities of the spacecraft, the satellite, and the planet. Errors in the satellite ephemeris may alias into estimation errors on the spacecraft state and/or the satellite gravity coefficients. As a consequence, satellite ephemerides must be updated as a part of the OD process. For the first iteration, the most recent ephemeris available is used. In subsequent iterations, the solution obtained from the previous iteration is used. Updated ephemerides are generated by integrating the full relativistic equations of motion of the planets and the satellites from their updated initial states. To compute the partials and update the ephemerides, the variational equations are integrated.

3.1.2.2.2 Integration of Equations of Motion and Variational Equations

Calculation of observables and their 'partials' requires reconstructing the spacecraft trajectory by integrating the equations of motion with respect to a nonrotating reference frame - which includes the coordinate system origin or Center Of Integration (COI) - from an initial state. The spacecraft Navigation Team usually provides the *a priori* reconstruction and associated uncertainties.

All non-negligible forces acting on the spacecraft (and the COI) must be modeled. In the general case, a spacecraft anywhere in the solar system, these may include:

- Point-mass Newtonian gravitational acceleration due to the Sun, major and minor planets and their satellites as well as asteroids and comets.
- Point-mass relativistic perturbing gravitational acceleration due to the Sun, the planets and the satellites of consequence.
- Acceleration due to geodesic precession.
- Acceleration due to Lense-Thirring precession.
- Newtonian acceleration due to the gravitational spherical harmonics of all planets and satellites, Pluto, and small bodies. The acceleration of the spacecraft relative to the COI due to oblateness of one of the bodies listed above is computed as the acceleration of the spacecraft direct component minus the acceleration of the COI indirect component. If the COI is also an oblate body, the acceleration of the COI is the sum of three terms: acceleration due to the spherical harmonics of the oblate body on the point-mass COI, acceleration due to the point-mass oblate body on the COI's oblateness, and acceleration due to the interaction between the oblateness of the body and the COI, although the third term may usually be neglected.
- Relativistic acceleration of the gravitational spherical harmonics: this effect is considered only for Earth's gravity field on a near-Earth spacecraft.
- Accelerations caused by tidal effects on the physical central body: the acceleration of the spacecraft derives from corrections to the central body's normalized harmonic coefficients due to the tides such as solid tides, ocean loadings, and pole tides.
- Acceleration due to time-varying gravity effects such as atmospheric or ice movement.
- Gravitational acceleration due to planetary rings.
- Gravitational acceleration due to mascons.
- Solar radiation pressure.
- Planetary radiation pressure: acceleration due to the radiation emitted from the surface of a planet, such as reflected visible light (albedo) and thermal emission.
- Thermal imbalance: acceleration due to non-uniform spacecraft surface heating.
- Gas leakage: acceleration due to spacecraft control jet leakage.
- Atmospheric drag.
- Maneuvers.

3.1.2.2.3 Time Transformations

Observables from ground tracking stations are time-stamped by the station clock. Apart from a small drift due to clock instability, the station reference time is equal to Coordinated Universal Time (UTC). However, for the light-time solution to be computed correctly, time must be expressed in Barycentric Coordinate Time (TCB). This is the coordinate time of the relativistic equations of motion in the solar system. Time can also be expressed as a linear transformation of TCB, such as Ephemeris Time (ET) or Barycentric Dynamical Time (TDB); ET is the independent variable of the JPL ephemerides.

3.1.2.2.4 Ground Station State Computation

The location of a ground station is conventionally defined as the position of a reference point whose coordinates are given as inputs in a terrestrial reference frame. The station location must be corrected to account for various effects:

- Solid Earth tides: the tides caused by the Moon and the Sun produce deformations of the Earth that change the location of the ground station. At least first order displacements and second order corrections due to a tidal potential of degree two due to both the Moon and the Sun must be considered. The first order displacement is about 50 cm, while the second order correction is about 13 mm. Usually the permanent tidal displacement is included in the expression of the first-order displacement, so the coordinates of the tracking stations must not include it.
- Ocean loadings: periodic displacements due to the periodic ocean tides. The displacements are less than 4 mm.
- Pole tide: the polar motion modifies the centrifugal potential of the Earth and causes a solid tide that produces a displacement of the tracking station. The displacement is less than 2 cm.
- Plate motion: a tracking station has a non-zero velocity due to tectonic plate motion. The station velocity due to plate motion can be up to 10 cm/yr.
- Offset between the real center of mass of the Earth and the origin of the considered terrestrial reference frame.
- Offset between the ground station's center reference point and phase center.

In order to solve the light-time equation, it is necessary to convert the station location from the terrestrial reference frame to the celestial reference frame. The transformation between the two reference frames consists of a series of rotations: polar motion, Earth rotation, nutation, and precession.

These rotations are characterized by a set of parameters that depend on the particular selected models. JPL group the EOP (section 2.5.2.1) that defines these rotations according to the International Astronomical Union (IAU) 1980 theory of nutation and the IAU 1976 precession model. After these rotations, the geocentric state of the tracking station is expressed in the geocentric space-time frame of reference, and it must be referred to the solar-system barycentric space-time frame of reference through proper Lorentz transformations.

3.1.2.2.5 Light-time Computation

The final part of the calculation is obtaining the light-time solution in the solar-system barycentric frame, which consists of the epoch of participation and the state of each direct participant at its epoch of participation. The direct participants for the light-time problem and the times of participation are:

- The receiving station at the reception time (t3).
- The spacecraft at the reflection time for two-way and three-way observables or transmission time for one-way observables (t2).

- The transmitting station at the transmission time for two-way and three-way observables (t1).

In the OD process, the reception time of an observable is known, so it is necessary to solve the light-time to find the transmission and the reflection times. The light-time problem is based upon the known speed of light and travel time from the transmitter to the receiver, which has two components:

- Newtonian light time that represents the time for light to travel along a straight-line path at the speed of light in a vacuum, *c*.
- Relativistic light-time delay, also called Shapiro effect, which accounts for the reduction of the coordinate velocity of light below *c* and the bending of the light path due to presence of a gravity field that curves the space-time.

The results of the light-time calculation are used to compute the values of observables at Earth tracking stations, as described by Moyer (2003).

3.1.2.3 **Estimation Filter**

The estimation filter computes parameter values that minimize the following in a least squares sense:

- Residual differences between the measured and computed observables. These are weighted by their measurement uncertainties; but, because the noise is not known prior to the first iteration, an *a priori* estimate based on available theoretical error budgets and experience is used. In the next iteration, the noise is estimated from the standard deviation of the residuals. It is held constant in subsequent iterations.
- Differences between the solve-for parameters and their *a priori* values are weighted using the uncertainty of the *a priori* information.

The estimation filter produces two outputs:

- A differential correction to *a priori* values of the solve-for parameters. It gives the updated estimate of the solve-for parameters.
- The covariance matrix of the solve-for parameters that represents the solution uncertainty. The *a priori* covariance matrix is updated based on the influences of measurement noises and consider parameter uncertainties on the solve-for parameters.

3.1.2.4 **Solution Analysis**

The solution obtained from the estimation filter is verified and tested using these criteria:

- Convergence: the OD process reaches convergence if two (or more) successive iteration steps produce statistically equivalent solutions.

- Residuals analysis: the obtained solution is used to compute residuals. If the OD process was performed correctly, the solution residuals represent only measurement noise, and hence must satisfy the following conditions:
  - Zero mean: the residual means must be much less than their standard deviations, *i.e*. compatible with a zero value.
  - Spectrum of residuals is compatible with the expected noise characteristics.
  - The residual standard deviations should be compatible with the residual weights used in the estimation filter.
- Solution covariance matrix analysis:
  - Comparison between *a priori* and computed formal uncertainties: a parameter is fully derivable from data if the computed uncertainties are much less than the *a priori* ones (typically, a factor 10 can be expected). Otherwise, the estimation depends importantly on *a priori* information and relatively less on measurements.
  - Cross-correlation between solve-for parameters: determine if any solve-for parameters are very strongly correlated.
- Comparison between *a priori* values and the new estimates: the new and old estimates of the solve-for parameters should be statistically compatible.
- Solution stability: to check the solution stability, it is useful to execute another estimation process using the solution as *a priori* values, with 'relaxed' increased *a priori* uncertainties. If the solution is stable, the new estimation will be statistically compatible with the testing solution.

3.1.3 Example: Rhea's Gravity Field from a Cassini Fly-By

Cassini's Rhea fly-by on November 26, 2005, provided data for estimation of the satellite's low degree gravity field by following the steps outlined in Section 3.1.2.

Data reduction was based on least squares filtering of the Doppler residuals that were generated by comparing measured sky frequencies with calculated values. The calculations depended on knowledge of the spacecraft state vector at the starting epoch and its dynamic environment, including:

- Motion of solar system bodies (planetary/satellite ephemerides)
- Ground station locations and Earth rotation dynamics
- Gravitational accelerations acting on the spacecraft — the central body's gravity and perturbations from other bodies
- Non-gravitational accelerations acting on the spacecraft
- Relativistic effects and the signal propagation model

3.1.3.1 Parameters

3.1.3.1.1 Solve-For Parameters

Solve-for parameters always include the spacecraft epoch state-vector x hours before close approach, the 3-D components of the spacecraft inertial position and velocity. It was also

necessary to solve for Rhea's initial state vector; errors in the satellite state could be aliased into the spacecraft state and the gravity coefficients. The minimum set of gravity coefficients contained the monopole and quadrupole fields — a total of 6 coefficients (*GM, J_2, $C_{2,1}$, $S_{2,1}$, $C_{2,2}$, $S_{2,2}$*). To reach degree 3 or higher would have required more fly-bys.

3.1.3.1.2 Consider Parameters

The *a priori* uncertainties (~10^{-9} m/s^2) of the RTG-induced acceleration (3-D components) and the thermo-optical properties of the spacecraft (which control the acceleration due to solar radiation pressure) cannot be inferred from flyby data, but they can be included as consider parameters.

3.1.3.1.3 Exact Parameters

A detailed model of Earth rotation was included to provide the correct inertial state of the ground stations. Typically, EOP data are obtained from the International Earth Rotation and Reference Systems Service (IERS). Perturbations due to the gravity of other solar system bodies (the Sun, Jupiter, Saturn, and other Saturnian satellites) were included.

3.1.3.1.4 *A priori* Uncertainties

Initializing the *a priori* covariance matrix of the solve-for parameters represents definition of *a priori* information in its own right. The covariance matrix is a full symmetric matrix - that is, it includes correlations between parameters. However, it is difficult to compute *a priori* correlations if previous data are not available. In this case, the covariance matrix was initialized to be diagonal.

A *priori* uncertainties must be carefully chosen so as not to constrain the parameter estimations. Knowledge of the Cassini state vector at the beginning of the fly-by was taken to be the trajectory reconstruction from the navigation team. *A priori* uncertainties in this case were set to 1 km (1-σ) for each position component and 3 mm/s (1-σ) for each velocity component, which are typical values.

3.1.3.2 Pre-processing of Radiometric Measurements

Doppler tracking of the spacecraft during the fly-by provided the measured observable — the time-dependent sky frequency, which is the frequency of the signal sent back by the spacecraft as it is received on Earth by the ground station. This frequency contained, among many other things, the Doppler shift caused by Rhea's gravitational influence on Cassini's fly-by trajectory.

3.1.3.2.1 Data Selection

Cassini tracking data could be acquired in either 2-way (F2) or 3-way (F3) mode. Carrier frequency options included X-band downlink coherent with X-band uplink (X/X) or Ka-band downlink coherent with X-band uplink (X/Ka). F2 is usually preferred over F3, since

the same frequency standard is used throughout the signal round trip time. X/Ka is usually preferred over X/X due to the former's higher immunity to plasma noise on the Ka-band downlink. In the 2005 Rhea flyby, a combination of these data types was available: F2 in X/X and X/Ka and F3 in X/Ka.

3.1.3.2.2 Data Compression

Each Doppler measurement is characterized by its count time. Compression, or averaging data over a larger count time, reduces the number of data points and associated noise. The maximum allowed count time depends on the time scale of the accelerations involved. For the Rhea case, when only low-degree harmonics were sought, count times as long as 60 seconds were used.

3.1.3.2.3 Group and Phase Delay Calibration

Corrections were applied to account for phase and time delays due to Earth's troposphere and ionosphere. Data from the AWVR were used to compensate for tropospheric effects (Section 2.5.2.3).

3.1.3.3 Calculation of Observables and Partials

Sky frequencies were calculated following the outline above. The spacecraft trajectory was computed numerically during each iteration using the then-current dynamical model.

3.1.3.4 Estimation Filter

Frequency residuals for a given iteration were obtained by comparing the observed sky frequencies with predictions based on the numerically computed trajectory integrated using the current dynamical model. The residuals were the main input to the data-filtering algorithm; the goal was to minimize the sum of squared residuals.

The pre-fit residuals were numerically computed starting from some *a priori* knowledge of the spacecraft state vector and dynamical model parameters. A plot of pre-fit residuals vs. time may show the effects of errors due to (1) observation noise, (2) unoptimized values of parameters of the mathematical model, and (3) inadequacies of the underlying models of the actual phenomena.

Figure 3-2a shows the pre-fit frequency residuals computed from the nominal dynamical model (a first guess of the dynamical environment of the spacecraft). The residuals contain signatures due to observation noise, errors in the mathematical model and errors in the values of model parameters. Errors in the dynamical model are particularly evident near closest approach (circled). Figure 3-2b shows the frequency post-fit frequency residuals. Fitted parameters have been updated with the least-squares solution, and the model trajectory fits the Doppler data extremely well.

3.3.3.5 Solution Analysis and Results

The Cassini spacecraft encountered Rhea on November 26, 2005, and analysis of the Doppler data acquired at and around closest approach yields the mass of Rhea and the quadrupole moments of its gravity field with unprecedented accuracy. Iess et al. (2007) obtained GM=153.9395+/-0.0018 km^3s^{-2}, which corresponds to a density of 1232.8+/-5.4 kg m^{-3}. The results for J_2 and C_{22} are $(7.947\pm0.892)\times10^{-4}$ and $(2.3526\pm0.0476)\times10^{-4}$, respectively. These values are consistent with hydrostatic equilibrium. From the value of C_{22}, they inferred the non-dimensional moment of inertia $C/MR^2=0.3721\pm0.0036$. Models of Rhea's interior based on the gravity data favored an almost undifferentiated satellite. A discontinuity between a core and a mantle is possible but not required by the data. Models with a constant silicate mass fraction throughout the body cannot account for the determined quadrupole coefficients. The data exclude fully differentiated models in which the core would be composed of unhydrated silicates and the mantle would be composed of pure ice. If the mantle contains 10% in mass of silicates, the core extends to 630 km in radius and has a silicate mass fraction of 40%. A continuous model in which the silicates are more concentrated toward the center of the body than in the outer layers is allowed by the gravity data but excluded by thermal evolution considerations. The one model that fits the gravity data and is self-consistent when energy transport and ice melting are qualitatively considered is an almost undifferentiated Rhea, in which a very large uniform core is surrounded by a relatively thin ice shell containing no rock at all.

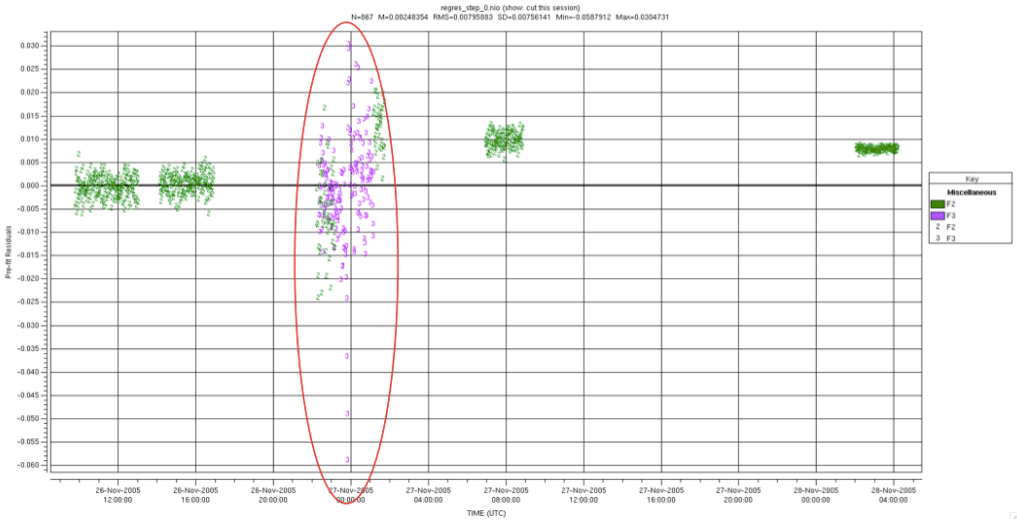

Figure 3-2a: Pre-fit residuals of a Rhea gravity experiment.

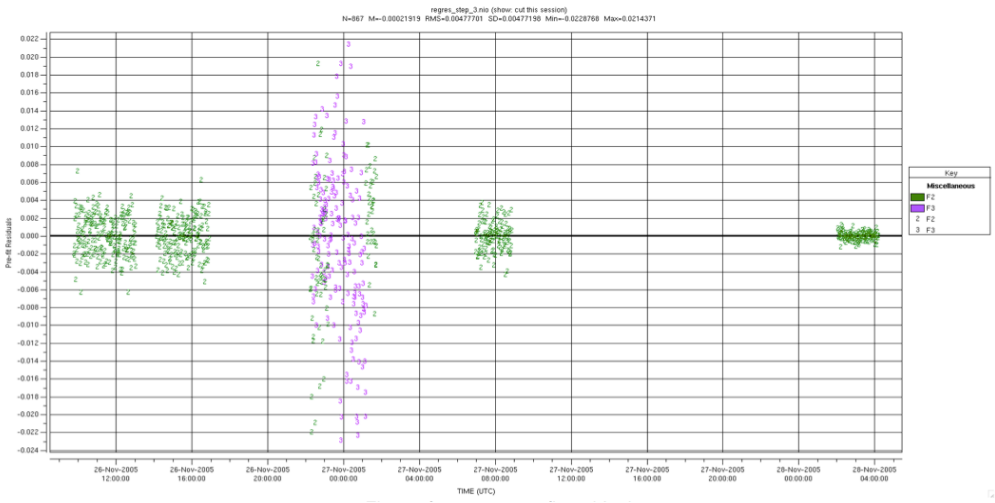

Figure 3-2b: Post-fit residuals of a Rhea gravity experiment.

3.2 **Atmosphere**

Almost all planetary missions have investigated planetary atmospheres and ionospheres using radio occultation techniques. The radio link is perturbed in phase and amplitude by the intervening plasma and/or neutral gas, and the perturbation measured on the ground can be converted into an atmospheric refractivity profile. The electron distribution in the ionosphere or temperature-pressure profile in the neutral atmosphere can then be derived from the refractivity.

The history of radio occultation studies goes back to the early 1960s. Von Eshleman of Stanford University first proposed the method in 1962. Independently, JPL's Dan Cain, studying the effects of refraction in the Earth's atmosphere on the accuracy of the observed Doppler, realized the potential for applying sensitive phase measurements to the study of the atmospheres and ionospheres of other planets (Kliore et al., 1964). Gunnar Fjeldbo (aka Lindal) (1964) advanced the theoretical technique during graduate research at Stanford and subsequent employment at JPL. These occultation techniques were demonstrated for the first time in 1965, when Mariner IV flew by Mars and determined the salient features of the Martian atmosphere. The observations showed that the surface pressure is less than one percent of Earth's — an order of magnitude less than had been previously believed (Kliore et al., 1965; Fjeldbo and Eshleman, 1968).

A radio occultation experiment was conducted using Mariner V during its flyby of Venus in 1967 (Kliore et al., 1965; Fjeldbo et al., 1971). In addition to acquiring the temperature-pressure profile in the neutral atmosphere and the electron density distribution in the ionosphere, Mariner V revealed that the Soviet Venera 4 spacecraft had not reached the surface of Venus (Kliore and Cain, 1968; Eshleman et al., 1968). Eshleman et al. (1977) and Tyler (1987) subsequently described radio experiments with Voyager; and Tyler *et al*. (1992) provided an overview of Mars experiments. Galileo experiments have been described by Howard *et al*. (1992), and the Ulysses Io plasma torus occultation experiment has been

described by Bird *et al*. (1992). Mariner, Viking, Pioneer, and Magellan experiments are cited below. Yakovlev (1985) described experiments on Soviet missions.

3.2.1 **Neutral Atmosphere**

The radio occultation technique relies on successful inversion of the observed changes in the frequency and amplitude of the radio signals during the atmospheric occultation period to produce vertical profiles of the index of refraction and absorption coefficient. For the case of spherical symmetry, where the atmospheric structure depends only on the radial distance from the center of the planet, the inversion technique has been firmly established. For the case of oblate planets, where the center of refraction is determined by the local radius of curvature at the occultation location, the spherical assumption provides a good first approximation.

In a one-way downlink experiment the ray between a spacecraft and a ground station is refracted in the planet's atmosphere, as shown in Figure 3-3. α is the bending angle and p is the ray asymptotic distance. ρ is the center of refraction. The position of the spacecraft when the photon was emitted is $\boldsymbol{r}_S$, and the position of the antenna on Earth when the photon was received is $\boldsymbol{r}_E$.

The experimental geometry is iteratively computed from the ephemerides of the spacecraft, the planet center, and the Earth center relative to the Sun, as well as the exact location of the receiving station relative to Earth's center. Knowledge of the spacecraft position and velocity, the assumption of spherical symmetry, and measurement of Doppler shift are combined to determine the bending angle as a function of ray asymptotic distance. This is then used to compute the refractivity profile of the atmosphere and, from that, a temperature-pressure profile.

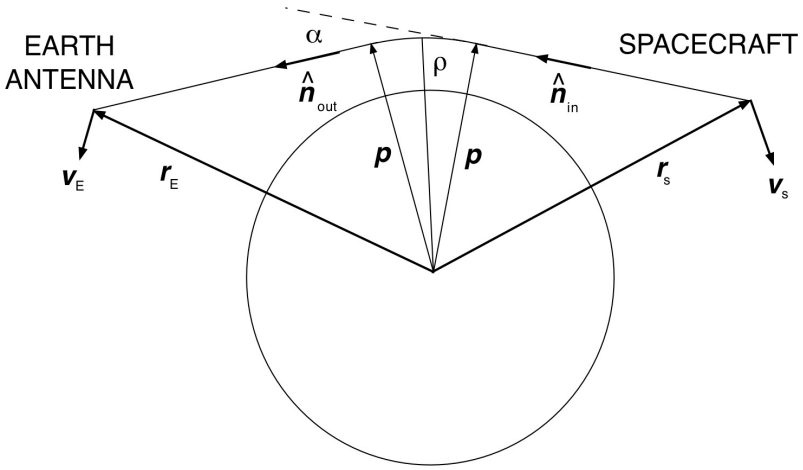

Figure 3-3. Geometry of a radio occultation observation.

Principles of such derivations are described in numerous references; Tyler (1987) is highly recommended as a starting point. The following sections outline the process of beginning

with occultation data recorded at a DSN station, incorporating ephemeris data from SPICE kernels, and producing a profile of the temperature as a function of altitude and pressure.

3.2.1.1 **Analysis**

To illustrate the steps in analyzing radio occultation data, we will use the Titan ingress occultation that took place during Cassini's orbit 113 on 22 June 2009 (T57I) (Schinder et al., 2012). Like all other Cassini radio occultations through 2011, this experiment was conducted in the one-way downlink mode using the spacecraft's USO as the onboard frequency reference. The USO failed in late 2011 and subsequent occultations were carried out in two-way mode, using a ground-based frequency reference. Because both the uplink and the downlink rays pass through the atmosphere under study, the two-way analysis is more complicated and will not be discussed here.

The Cassini RS Team uses two different numerical techniques to invert one-way data. The more general technique is ray tracing, which uses geometrical optics to trace rays from the spacecraft to the receiving antenna, simultaneously solving for the structure of the atmosphere as each successive ray is traced. When the target atmosphere is spherically symmetric, a much faster and simpler Abel transform directly connects the bending angle between the ray leaving the spacecraft and the ray arriving at the ground station with the index of refraction of the gas. The Abel technique is used for Titan occultations while ray tracing is used for Saturn occultations because Saturn is significantly oblate and its atmosphere supports planetary scale zonal winds, which further complicate the atmospheric structure. We caution others against using a spherical approximation for Saturn atmospheric occultations except as an initial step in those analyses. Lindal (1992) lays out the technique for an oblate body. He assumes solid body rotation for the atmosphere. The Cassini team allows a restricted (barotropic assumption) differential wind field (Flasar and Schindler – in preparation).

3.2.1.1.1 **Converting Raw RSR Data to Usable Forms**

Prior to the failure of the Cassini USO, the spacecraft could transmit simultaneously at three USO-driven frequencies in the S-, X-, and Ka-bands. Each of these frequencies is considered to be constant in the spacecraft's rest frame, and each can be used for radio occultation either independently or together with one or two of the others.

As any of the three signals is received at a ground station, it is immediately mixed with a DSN fixed-frequency local oscillator signal that down-converts it from the GHz range to the 300 MHz range and delivers it to an RSR (see section 2.5.1.3), where the output is digitized and a programmable local oscillator down-converts the frequency again to the 0 - 100 kHz range.

The tunable local oscillator frequency (sometimes known as the 'steering' frequency) is generated from an RSR frequency prediction file, which is pre-computed by the RSSG using a model of the atmosphere and the predicted ephemeris of the spacecraft provided by the spacecraft navigation team. The open-loop recording is typically at sampling rates of 1

kHz to 100 kHz, depending on the specific experiment design. The resulting time series of antenna voltages is contained in the RSR output file along with the steering frequency in the form of piecewise polynomials (see Section 2.3.2.1.2).

For an occultation done in two-way mode, there is an additional pre-computation necessary. We use a model atmosphere and a predicted ephemeris to compute the *uplink frequency* to be sent from a ground station. The paths followed by the uplink and downlink signals through the atmosphere are very similar (but not identical). We use the model atmosphere to compute the frequency that needs to be transmitted so that, as nearly as possible, the spacecraft sees a constant uplink frequency in its own frame.

The first step in obtaining the structure of an atmosphere is reconstruction of the 'sky frequency,' the frequency of the signal received by the DSN antenna prior to any down-conversion. A Fast Fourier Transform (FFT) algorithm or digital phase-locked loop (PLL) is used to extract the signal frequency from the recorded antenna voltages. Although 'steering' has compensated for most of the large changes, some residual remains; and this (raw) residual contains critical parts of the science measurement. The raw residual is then combined with the two local oscillator frequencies and appropriate multipliers, offsets, and sign changes that mathematically model the signal path through the receiving system to give the sky frequency at S-, X-, or Ka-band (Section 2.3.2.1.2).

The time and frequency resolutions of an FFT (or PLL) calculation are inversely related to each other. Fortunately, the effect of the target's atmosphere on the received signal is often substantial; in most cases a nominal choice for time and frequency resolution is satisfactory. However, Titan occultations occur quickly (on the order of hundreds of seconds) and the signals are dynamic; high time *and* frequency resolution are both desirable. Although high accuracy in signal strength is needed to estimate absorption after correction for refractive defocusing, optimizing the time/frequency resolution pair is the first priority.

Frequency resolution of the FFT depends on the number of points and the sampling rate; there are several ways to optimize the time/frequency resolution process, although none actually improves the information content of the result. (1) If an FFT is used to obtain an initial estimate of signal frequency, a Continuous Fourier Transform (CFT) may be used to improve the apparent precision of the estimate. (2) Zero padding - adding zeroes to a sample stream to make it appear longer - may be used to improve frequency resolution at the expense of spectral artifacts from the padding. (3) FFT averaging can be used to improve accuracy of signal strength estimates when the signal level is approximately constant. For example, an average of 16 consecutive power spectra reduces the uncertainty of the power in each frequency bin by a factor of 4 (but at a cost of a factor of 16 in time resolution). (4) A sliding FFT, in which some time samples from the previous FFT are re-used in the new FFT, can give the appearance of a smoother time sampling of FFT output. For example, a series of 512-point transforms in which the latest 448 time samples are re-used in each new FFT gives the appearance of 8 times higher sampling, but only every 8th output value is independent. (5) It is also possible to slide the averaging window — for example, dropping one spectrum while adding a new one when computing a running average over 8 successive power spectra. (6) Sample sizes longer than 512 points can be used, at the cost

of decreasing the time resolution. This increases the frequency resolution. By using a sliding data window, the time resolution can be the same as using 512 points, at the cost of introducing correlations between the frequency points.

Figure 3-4 shows the T57I signal frequency obtained by using 8x512-point FFTs (16 kHz sampling) and method (5). Nominal frequency resolution of the 8x512 spectrum was 3.9 Hz, which was further improved by using a CFT to a nominal resolution of 1 mHz. Independent signal strength and frequency estimates were obtained every 0.256 s; but, because of the sliding data window, values were generated every 0.032 s. The averaging improved the accuracy of the SNR, but signal dynamics with characteristic time scales less than 0.256 s were lost.

Figure 3-4 shows that the steering worked very well; the offset of approximately 10 Hz in this case is typically the result of small errors in the prediction ephemerides and will become insignificant once the actual state vectors are calculated (see next sections).

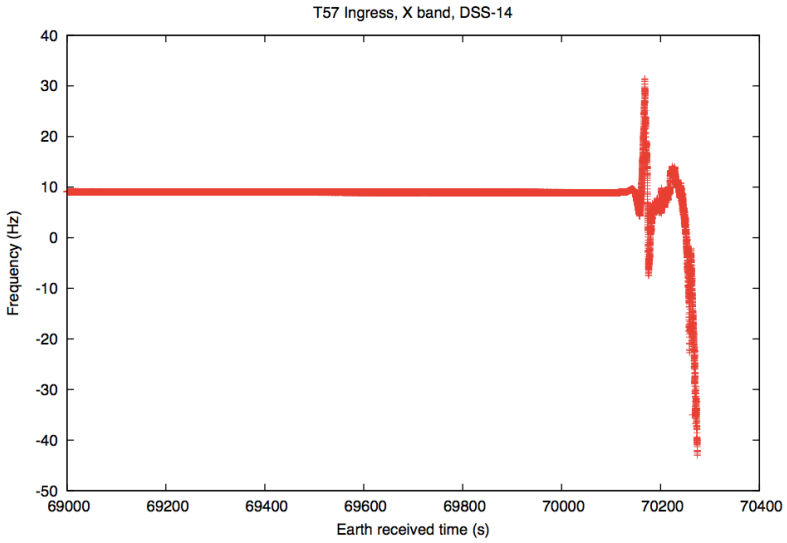

Figure 3-4: Frequency of the Cassini carrier at the output of the X-band RSR during the T57I occultation ingress observation. RSR complex samples (I/Q pairs) were recorded at 16 kHz (file S51TIOI2009173_1845NNNX14RD.1A2). Data were processed using 512-point FFTs, with running averages over 8 transforms slipped by one transform per calculation (0.032 s per output point, 0.256 s per independent point). Horizontal axis gives time since UT midnight in seconds at the DSS-14 receiving antenna.

3.2.1.1.2 **Using the Ephemeris**

The next step in the processing is to use the highest quality spacecraft and planetary ephemerides to reconstruct the geometry of the occultation and to determine the bending angles that correspond to the frequencies observed on the ground. The ephemeris for the Cassini mission is in the form of SPICE kernels, which can be used with the NAIF toolkit (ftp://naif.jpl.nasa.gov/pub/naif/toolkit), a suite of routines users can incorporate into their own analysis software. The SPICE kernels for the Cassini mission

(ftp://naif.jpl.nasa.gov/pub/naif/CASSINI/kernels) are in binary or text format, and different kernels contain information about various bodies. For example, the SP kernels are binary files containing the position and velocity state vectors for Saturn, its satellites, the Sun, the Earth, and the spacecraft. PC kernels are text files containing the masses and rotational parameters for various bodies. For the analysis of the T57I occultation, we used:

```
KERNELS_TO_LOAD=(
'100209AP_RE_90165_18018.bsp',
'naif0009.tls',
'cpck17Aug2009.tpc',
'090806R_SCPSE_09168_09184.bsp',
'Earthstns_itrf93_050714.bsp',
'Earth_031228_231229_predict.bpc' )
```

We began with an observed frequency point well outside the atmosphere and used (after Lindal, 1992):

$$f_s = f_r \left(\frac{\left(1 - 2\Phi_s - \boldsymbol{v}_s \cdot \hat{n}_{in}/c\right)}{\left(1 - 2\Phi_E - \boldsymbol{v}_E \cdot \hat{n}_{out}/c\right)} \frac{\sqrt{1 - 2\Phi_E - \left(|\boldsymbol{v}_E|/c\right)^2}}{\sqrt{1 - 2\Phi_s - \left(|\boldsymbol{v}_s|/c\right)^2}} \right) \tag{3}$$

where f_s is the spacecraft transmitted frequency and f_r is the received frequency for the same photon one light time later. Note that all subsequent mention of 'transmission' and 'reception' implies observation of the same photon with light time corrections applied; passage of the photon through the atmosphere of Titan requires a small light time adjustment from transmission. $\boldsymbol{v}_s$ is the spacecraft velocity at the time of transmission (Figure 3-3), $\boldsymbol{v}_E$ is the velocity of the receiving antenna at the time of reception, Φ_E is the gravitational potential at the receiving antenna including the potentials of the Earth and the Sun, and Φ_s is the gravitational potential at the spacecraft, including Saturn, Titan, and the Sun. $\hat{n}_{in}$ is a unit vector tangent to the ray path as the photon leaves the spacecraft, and $\hat{n}_{out}$ is a unit vector parallel to the ray path when the same photon arrives at the receiving antenna one light-time later; in vacuum $\hat{n}_{in} = \hat{n}_{out}$, a condition which will not be true once the ray path enters the atmosphere. The dimensionless potential $\Phi = GM/Rc^2$, where M is the appropriate mass and R the appropriate distance. In the case of Titan, Φ_s contains the sum of the potentials of Titan, Saturn, and the Sun at the position of the spacecraft.

Equation 3 was applied to each successive frequency. Instead of solving for f_s, we used the initial f_s to solve for the frequency we predicted to be received f_r. This prediction was subtracted from each measured sky frequency, creating *Doppler residuals*. Since the spacecraft emitted a constant frequency in its rest frame, f_s should be the same throughout the occultation, and the Doppler residuals should ideally be zero until the atmosphere is reached. In practice, the ephemeris contains small errors, the path between the spacecraft and the DSN antenna is not quite a vacuum, the USO has a small drift, and the ray path traverses the atmosphere of the Earth; so there are small deviations from the ideal. Figure 3-5 shows the Doppler residuals obtained from T57I in X-band at DSS-14 after correction for ephemeris errors, USO drift, and effects from Earth's atmosphere.

The T57I Doppler residuals have a very stable free-space baseline with no significant deviation from zero outside the atmosphere. More typically there are linear drifts on the order of 10^{-4} Hz per second, and occasionally some curvature is seen. Uncorrected systematic deviations from zero Doppler residual can produce unphysical structure in the retrieved atmospheric structure. To protect against such errors, we chose a *baseline* of points that are clearly unaffected by the atmosphere (in this case, between 69000 and 69800 s Earth Received Time (ERT)), integrated the Doppler residuals in time to obtain a phase profile, and then fitted the phase with a cubic polynomial as a function of ERT. The fit was then removed from the entire frequency record (not just the baseline). At the same time, the fit provided f_s, the spacecraft oscillator frequency (alternatively, one may fit a quadratic to the Doppler residuals themselves and get the same answer, but we have traditionally used the phase). Once the de-trending had been completed, it was possible to carry out the inversion to obtain the atmospheric temperature-pressure profile that is consistent with the observed frequency record.

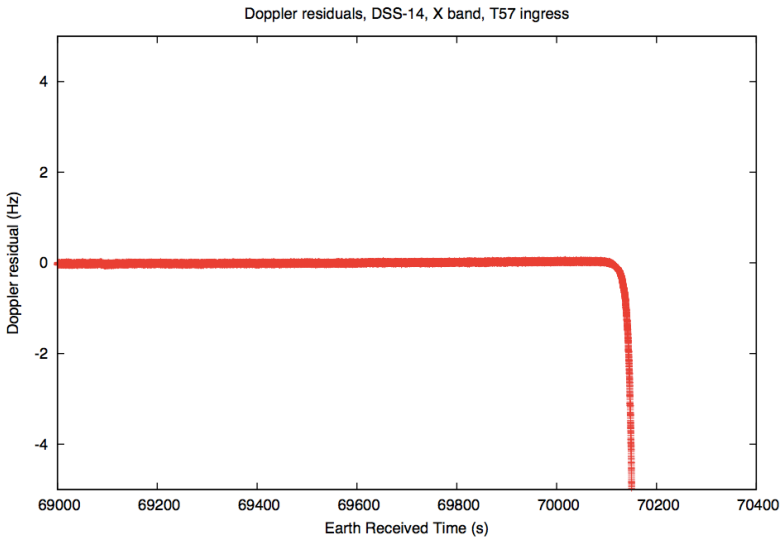

Figure 3-5: Doppler residuals for T57I, DSS-14, X band.

3.2.1.1.3 Abel Inversion

The assumption of spherical symmetry imposed upon the atmosphere of Titan greatly simplifies the analysis task. The inversion is then analogous to a central force problem in celestial mechanics. The 'force' is the gradient of the index of refraction $n(r)$, assumed by spherical symmetry to be a function solely of the radius r, which tugs on the ray and changes its direction as it traverses the atmosphere. Because the force is central, each successive ray is confined to a plane containing the spacecraft, the center of Titan, and the receiving DSN antenna on Earth. Successive ray paths will be in different planes because the spacecraft and DSN antenna are continually moving; however, planar geometry can be used to obtain the bending angle within each plane. With the assumption of spherical symmetry, it can be shown (Phinney and Anderson, 1968) that there is a unique Abel transform relating the bending angle to the refractivity of the atmosphere. There is an analog of total angular momentum conservation with which we can obtain the minimum radius of the *ray*

periapsis R without ever determining the actual ray trajectory. Indeed, the path of the ray is neither required nor determined using this method.

The Abel integral relates the refractivity and bending angle (defined above) to the impact parameter a, which is the product of radius R and index of refraction n at the ray's closest approach. The bending angle α is computed from the geometry and the Earth-received frequency by invoking several conditions. The primary condition, which can be imposed because of the spherical symmetry, is that the ray trajectory remains in a single plane; that plane is defined by the spacecraft, the center of the target, and the receiving DSN antenna. The angle between the spacecraft velocity vector $\boldsymbol{v}_s$ and the initial ray direction $\boldsymbol{n}_{in}$ is determined from the frequency recorded on the Earth. The ray must eventually intersect the DSN antenna so it can be recorded.

The unit vector perpendicular to the solution plane is

$$\hat{z} = \frac{r_s \times r_E}{| r_s \times r_E |} \tag{4}$$

where $\boldsymbol{r}_s$ is the vector position of the spacecraft, and $\boldsymbol{r}_E$ is the position of the receiving antenna both with respect to the target. Both can be derived from the ephemeris by solving the light time equation.

Some conditions can be imposed on the unit vector in the initial direction of the ray. First, it can be constrained to lie upon a known cone because we know both the Earth received frequency and the velocity of the spacecraft:

$$v_s \cdot \hat{n}_{in} = | v_s | \cos\beta \tag{5}$$

where $\cos\beta$ is determined from the frequency record by:

$$| v_s | \cos\beta = -\left(\frac{f_s}{f_r}\left(1 - v_E \cdot \hat{n}_{out}\right) - 1 \right) \tag{6}$$

Here, f_s is the spacecraft oscillator frequency in its rest frame, f_r is the frequency recorded at the antenna, v_E is the velocity of the antenna, and $\hat{n}_{out}$ is the (to be determined) unit vector in the final direction of the ray after it has passed through the atmosphere (second-order relativistic effects are included in our analysis code, but are relatively small and are omitted in this description for clarity). The other condition that can be immediately imposed is that $\hat{n}_{out}$ is perpendicular to p.

Additional constraints are provided by considering the vector that is perpendicular to the outgoing ray asymptote. The vector $\boldsymbol{r}_E$ from the center of the target to the antenna on the Earth and the vector $\boldsymbol{p}$ from the center of the target to the point on the outgoing ray asymptote such that $\boldsymbol{p}$ is perpendicular to the asymptote, satisfies the following conditions:

$$r_E \cdot p = p^2$$

$$p \cdot p = \mathrm{p}^2 \tag{7}$$

$$\hat{z} \cdot p = 0$$

p is the impact parameter, which can be determined geometrically. Since the ray path must be symmetric about the origin, the impact parameter for the incoming ray must be the same as that for the outgoing ray. The spacecraft's velocity vector is projected onto the ray plane:

$$v_s' - v_s - (v_s \cdot \hat{z})\hat{z} \tag{8}$$

The angle between the spacecraft's velocity vector and its radius vector is:

$$\gamma = \cos^{-1}\left(\frac{v_s' \cdot r_s}{|v_s'||r_s|}\right) \tag{9}$$

Then

$$\mathrm{p} = |r_s| \sin(|\alpha - \gamma|) \tag{10}$$

With this background, the reader should be well equipped to apply the subsequent analysis described in Schinder *et al*. (2012), resulting in the solution of six non-linear equations to obtain an expression for the bending angle,

$$\alpha = \cos^{-1}(\hat{n}_{\mathrm{in}} \cdot \hat{n}_{\mathrm{out}}) \tag{11}$$

We use the following form of the integral from Lipa and Tyler (1979) to compute the index of refraction as a function of the impact parameter:

$$n(\mathrm{r}) = \exp\left[\frac{1}{\pi}\int_{\mathrm{r}}^{\mathrm{r_1}} \ln\left(\frac{\mathrm{p}}{\mathrm{p_1}} + \sqrt{\left(\frac{\mathrm{p}}{\mathrm{p_1}}\right)^2 - 1}\right) \mathrm{d}\alpha(\mathrm{r})\right] \tag{12}$$

Here, n(r) is the index of refraction and p_1 is the impact parameter of the 'surface' of the atmosphere or ionosphere, a point outside of which the index of refraction is assumed to be zero; r, the radius of the ray periapsis, the closest point on the ray to the surface of Titan, found by an analog to angular momentum conservation $r=p/n$.

The refractivity N is related to the index of refraction by $N = (n\text{-}1)\ \mathrm{x}10^6$. Once the atmosphere's radial refractivity profile has been determined, the temperature and pressure as a function of altitude are easily computed. We assume that Titan's atmosphere is primarily N_2 with a small admixture of CH_4 that is constant throughout the atmosphere and is 0.014 by number. The density of the atmosphere is

$$\rho = \frac{f_{CH_4} M_{CH_4} + f_{N_2} M_{N_2}}{f_{CH_4} r_{CH_4} + f_{N_2} r_{N_2}} m_A N \tag{13}$$

where f_{CH4}=0.014 is the fraction of CH_4 by number, f_{N2}=1- f_{CH4} is the fraction of N_2 by number, M_{CH4}=16.0426 is the mass of CH_4 in atomic mass units, M_{N2}=28.006 is the mass of N_2 in atomic mass units, m_A=1.66053x10^{-24} gm is the atomic mass unit, r_{CH4}=1.63x10^{-17} is the refractivity per molecule of CH_4, and r_{N2}=1.1x10^{-17} is the refractivity per molecule of N_2. Once the density is found, hydrostatic equilibrium

$$\frac{dP}{dz} = -g(z)\rho(z) \tag{14}$$

and an equation of state can be used to find the temperature profile. We adopt the Bender equation of state for Titan's atmosphere (Bender, 1973), which is more realistic than the ideal gas law for N_2 at such low temperatures. Finally, we obtain the temperature-altitude profile shown in Figure 3-6. Note that the absolute temperatures obtained from using the ideal gas law would be several K different from these results.

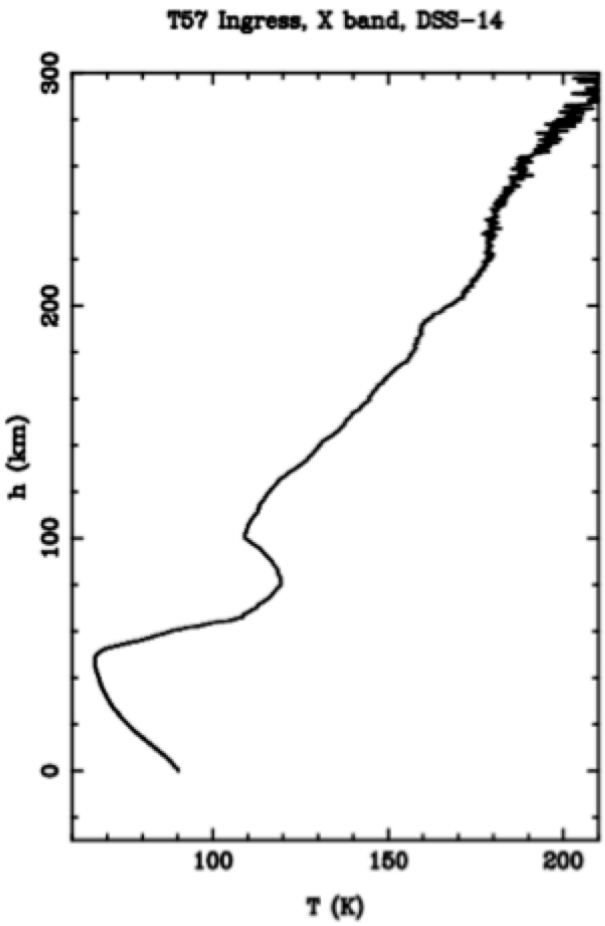

Figure 3-6: Temperature - altitude profile for T57I, using the Bender equation of state.

3.2.2 **Ionosphere**

The atmospheric radio occultation technique described in the preceding section also applies to investigations of ionospheric layers. Charged particles interact with the propagating signal in a dispersive manner, i.e., as a function of the signal's wavelength. Thus, occultation experiments using two or more transmitted frequencies are ideal for ionospheric occultations since the dispersion can be characterized by differencing the signals. All non-dispersive effects in the Doppler profile, such as trajectory and gravitational and non-gravitational forces and errors, drop out in the differencing. For ionospheric occultations, Doppler data are typically available through the closed-loop tracking system of the DSN. However, better data quality and flexibility in processing favor the use of open-loop RSR measurements. The processing steps to convert from raw RSR data samples to ionospheric density profile are summarized below.

3.2.2.1. **Signal Detection in the RSR**

Either a user-supplied Fast Fourier Transform (FFT) or digital phase-locked loop (PLL) is first applied to the data to determine the recorded signal's frequency and power as a function of time within the RSR output sample steam

3.2.2.2. **Conversion of Recorded Frequency to Sky Frequency**

The steering function of the RSR (described previously) is included in the recording and these values are added to the RSR frequencies to obtain the sky frequency, the actual frequency sensed by the receiving antenna. The steering compensates for the RSR tuning and follows predictions generated in advance based on the predicted spacecraft trajectory.

3.2.2.3. **Conversion of Sky Frequency to Residuals**

Residuals are the differences between measured frequencies (the sky frequencies) and the calculated frequencies based on values of all known contributing factors after the fact. The calculation parallels the calculation used in deriving the steering values but it uses the best a posteriori spacecraft trajectory, Earth rotation, solar system ephemerides, and USO frequency, This can be done by using spacecraft trajectory information contained in the SPK kernels provided by the Cassini Navigation Team and USO test results acquired separately from science observations. It is best to create a model of the sky frequency profile from the SPK file and then difference it from the observed profile to generate the residuals containing the science information.

3.2.2.4. **Extraction of the Ionospheric Profile**

Once the signal frequency, frequency residuals, power and spacecraft trajectory data are available for a given occultation, standard techniques can be applied to determine the ionospheric profile of the atmosphere. In its simplest form, ionospheric analysis does not require an inversion process, and is much more straightforward than neutral atmospheric analysis.

For example, Kliore e*t al.* (2008) show the ionosphere of Titan; see Figure 3-7. The first four sets of radio occultations of the Titan's ionosphere were obtained by the Cassini spacecraft between March 2006 and May 2007. These occultations occurred at middle and high latitudes, at solar zenith angles from about 86° to 96°. The main ionospheric peak was seen, as expected from modeling and previous observations, near 1200 km, with a density of about 1–3 × 103 cm−3. A consistent ledge near 1000 km was also seen, and one of the polar observations found a significant (~3 × 103 cm−3) layer in the region of 500–600 km. This layer also is seen in other observations with a density varying from about 0.7 to 1.7 × 103 cm−3, suggesting a variable production source (or sources) for this peak.

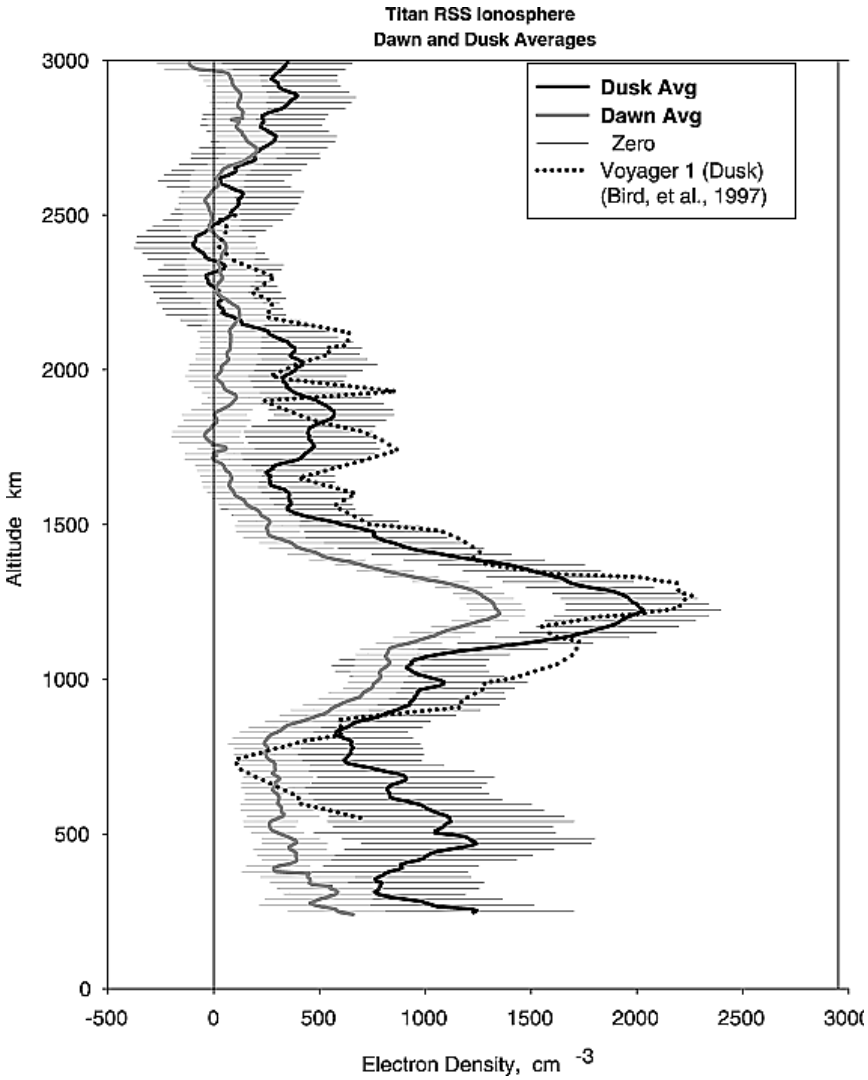

Figure 3-7: From Kliore et al., 2008, observed dawn and dusk and dawn averaged electron density profiles. For T12 and T14 (southern mid latitudes), the dusk observations are also in sunlight, and the dawn observations are in the dark. The Voyager 1 profile is also shown for comparison.

3.3 **Rings**

3.3.1. **Overview**

During a ring occultation observation, Cassini transmits three coherent sinusoidal signals simultaneously through the rings. They are generated from the common onboard USO, allowing measurement of their amplitude, frequency, and phase, as well as their relative phases. Their approximate wavelengths are given in Table 1-1.

We follow Marouf and Wong (2012) and Marouf *et al*., (1982, 1983), in describing ring occultation data processing. At the DSN complex, a 70-m station is usually used to receive

the X- and S-band signals. A 34-m station is used to receive the Ka-band signal and X-band as a backup. For any given band, the received signal can be modeled as a narrow-band signal of the form

$$s(t) = I_m(t)\cos(\omega_c t) - Q_m(t)\sin(\omega_c t) = \mathrm{Re}\{[I_m(t) + iQ_m(t)]\exp(i\omega_c t)\} \qquad (15)$$

where ω_c is assumed to be known. The signals are down-converted in frequency to the center of the recording bandwidth, *BW*. Typical sampling rates used for ring occultations are 1, 16, and 50 kHz. The RSR encodes and preserves full information about the values of local oscillator frequencies used for the down-conversion, so that sky frequency may be recomputed after the fact.

The recorded (measured) samples encode the $I_m(t)$ and $Q_m(t)$ values using a uniform time grid. The pair (I_m, Q_m) can be modeled by the complex number

$$I_{\mathrm{m}}(\mathrm{t}) + iQ_{\mathrm{m}}(\mathrm{t}) \qquad (16)$$

and the samples are usually referred to as the measured complex signal. ERT UTC is used for time tagging the samples. The time history of the complex signal during an occultation provides valuable information regarding ring structure and particle physical properties.

3.3.2. **Observables**

As a transmitted signal passes through the rings, the ring material perturbs it. Two signal components can be identified in the measured spectrum of the perturbed signal (see Figure 3-8). The first is the direct signal, a narrow spectral line that is the remnant of the coherent incident sinusoid after being attenuated and phase shifted by ring material. The time histories of estimated average power and phase change of the direct signal provide a measured extinction and phase shift profile. The extinction is characterized in terms of an optical depth and, with the help of a reconstructed spacecraft trajectory, is used to compute an optical depth versus radius profile of the ring system as a function of wavelength. The initial profile is diffraction-limited. Accurate measurement of the signal phase allows reconstruction of the profile to remove diffraction effects (Marouf *et al*., 1986).

The second component is the near-forward scattered signal, a frequency-broadened signal that originates from incoherent superposition of the signals scattered by ring particles located within the intersection of the main-lobe of the Cassini high-gain antenna and the rings plane (antenna footprint). The Doppler shift caused by the relative motion of the spacecraft, ring particles, and ground station broadens the spectrum of this signal component. The time history of the scattered signal spectra (Figure 3-9) can be used to determine the size distribution of large (> 1 meter) particles as well as other physical properties (Marouf *et al.*, 1983; Zebker *et al.,* 1985).

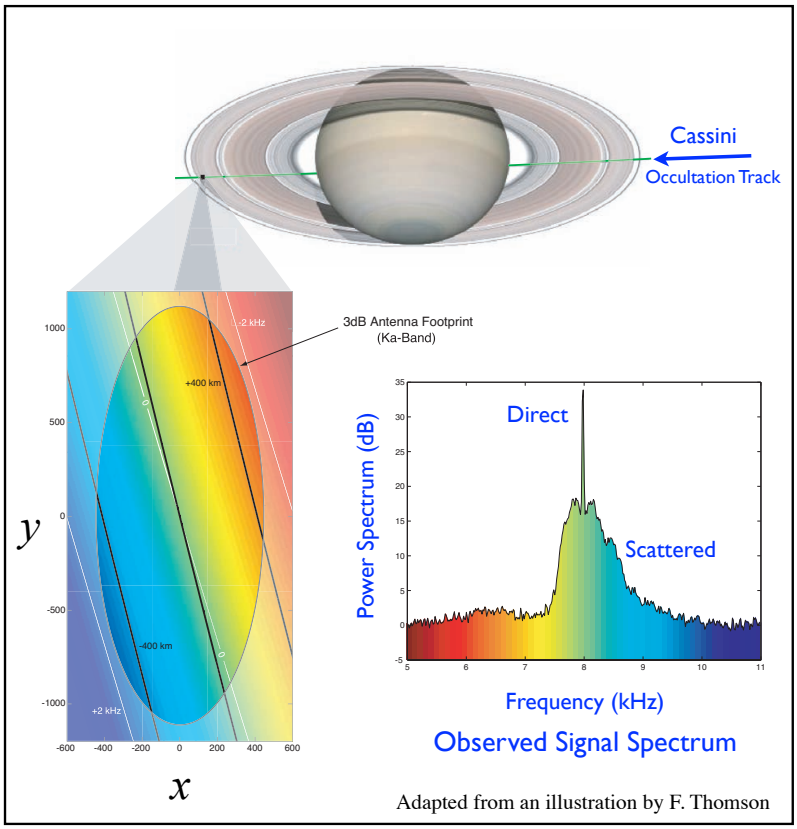

Figure 3-8: Illustration of ring radio occultation direct and scattered signal, and of Doppler mapping over the Ka-band 'footprint' of the Cassini high-gain antenna.

3.3.3. **RSS Ring Occultations During the Cassini Prime Mission**

Twenty-four one-sided radio occultations of Saturn's rings were observed during the Cassini Prime Mission (Table 3-1); additional experiments since the prime mission are listed in Appendix 1 online (see the URL in section 1.0). The spacecraft trajectory is chosen so that the path of the radio signals transmitted from Cassini to an observing ground receiving station would be interrupted by the ring system.

The Prime Mission occultation observations sampled a broad range of ring opening angles, *B*. In particular, a set from Revs 7 to 14 of mostly diametric occultations captured relatively large angles, 19.5-23.5°, allowing detailed profiling of the optically thick Ring B for the first time. Another set from Revs 53-67 of mostly chord occultations sampled small |*angles,* 6-10°. The limited intermediate range of angles, 14-15°, was sampled by occultations from Revs 28, 44, and 46. These 24 occultation cuts also sampled a broad range of ring longitudes both inertial and Earth-relative.

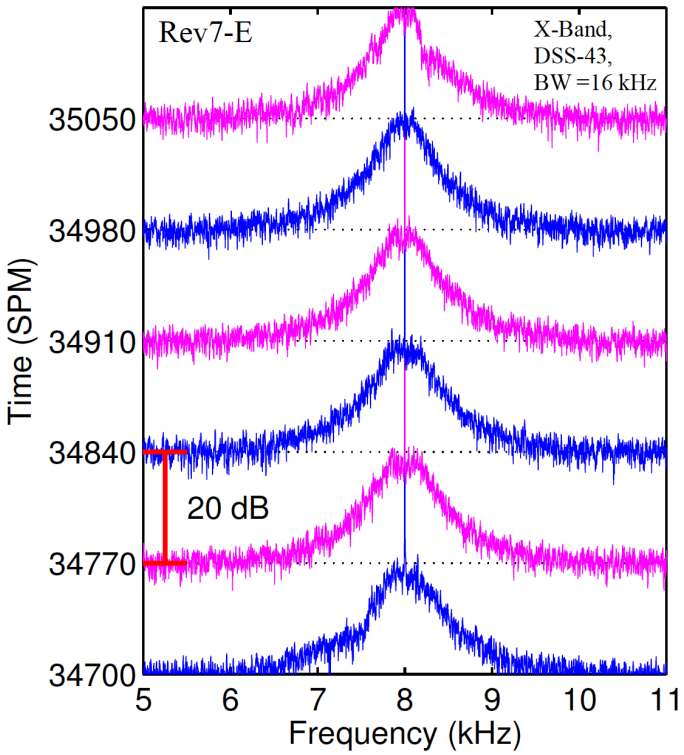

Figure 3-9: Example time sequence of Ring A spectra used to estimate the frequency offset of the direct signal from the center of the recording bandwidth. SPM is seconds past midnight on 2005-05-03.

3.3.4. **Analysis**

Reliably extracting ring structure from the recorded data requires reliable estimation of the variations in phase of the direct sinusoidal signal and amplitudes of the direct and scattered signals as functions of time.

3.3.4.1. **Frequency Calibration**

Accurate estimation of the signal phase requires compensating the phase from the acquired complex samples for any deterministic offset of the frequency of the direct signal from its expected position at the center of the recording bandwidth. This is accomplished by compensating the phase of the measured I/Q samples as follows:

$$I_c(t) + iQ_c(t) = \left[I_m(t) + iQ_m(t)\right] \exp\left[-i\psi(t)\right] \tag{17}$$

where the phase function $\psi(t)$ is computed from

$$\psi(t) = \int^t \hat{f}_{offset}(\tau)\, d\tau + \psi(t_0) \tag{18}$$

$\hat{f}_{\text{offset}}(t)$ is an estimate of the frequency offset, and $\psi(t_0)$ is an arbitrary constant. Usually, a large fraction of $\hat{f}_{\text{offset}}(t)$ comes from inaccuracies in the predicted spacecraft trajectory used to compute the predicted Doppler shift $f_{\text{dp}}(t)$ needed to tune the RSR (see section 2.3.2.1). A spacecraft trajectory reconstructed after the experiment can be used to compute a more accurate Doppler shift, $f_{\text{dr}}(t)$. The difference is used as part of the estimate above. We use $\hat{f}_{\text{resid}}(t)$ to denote any remaining residuals:

$$\hat{f}_{\text{offset}}(t) = \left[f_{\text{dr}}(t) - f_{\text{dp}}(t) \right] + \hat{f}_{\text{resid}}(t) \tag{19}$$

Table 3-1
RSS Ring Occultations Completed During Cassini Prime Mission

Occ #	YYYY-DOY(1)	Cassini Rev#	Ingress/Egress /Chord	*B* (deg)(2)
1	2005-123	7	I	-23.57
2	2005-123	7	E	-23.57
3	2005-141	8	I	-23.17
4	2005-141	8	E	-23.17
5	2005-159	9	E	-22.64
6	2005-177	10	I	-22.01
7	2005-177	10	E	-22.01
8	2005-196	11	E	-21.29
9	2005-214	12	I	-20.54
19	2005-214	12	E	-20.54
11	2005-232	13	E	-19.76
12	2005-248	14	I	-19.12
13a(3)	2006-258	28	I	-14.35
13b(3)	2006-259	28	I	-14.35
14	2007-130	44	E	-15.23
15	2007-162	46	I	-14.37
16	2007-337	53	I	-6.68
17	2007-353	54	C	-6.63
18	2008-015	56	C	-7.04
19	2008-027	57	C	-7.38
20	2008-039	58	C	-7.80
21	2008-062	60	C	-8.65
22	2008-092	63	C	-9.60
23	2008-102	64	C	-9.79
24	2008-130	67	C	-9.91

Notes: (1) Observation Year and Day-of-Year. (2) Ring opening angle. (3) Ingress occultation was interrupted over Ring B by a high-phase orbiter remote sensing observation.

To illustrate the analysis, we use the Cassini egress ring occultation Rev7-E; see Table 3-2 for a list of files used in processing. A sequence of power spectra is derived from the measured $I_m(t) + i\,Q_m(t)$ samples; a representative subset of those spectra is shown in Figure 3-9, where both the direct to Earth and scattered signal components are clearly visible.

Each spectrum is searched for the frequency of its peak value near the center of the recording bandwidth; this peak is presumed to be the direct signal, but it can be scattered signal or noise where the ring has large optical depth.

Least squares fitting of model spectra of sinusoidal signals to the measured spectral values around the peak can be used to refine the position of the peak (Lipa and Tyler, 1979). The desired $f_{\text{offset}}(t)$ is then computed as the offset of the estimated peak frequency from the center of the recording bandwidth (BW = 1 kHz in this case; see Table 3-2). The noisy green curve in the upper panel of Figure 3-10 depicts $f_{\text{offset}}(t)$ computed for Rev7-E over a time span that covers Rings C, B, then A, followed by a free-space baseline. The estimated profile is very noisy and almost random in optically thick regions of Ring B; it is less noisy in Ring A, and it is much less noisy in Ring C, the Cassini Division, and outside Ring A.

Table 3-2: Rev 7-E Input Data Files

Observing DSN station: DSS-43 Frequency band: X-Band Date: 2005-05-03 (2005-123) *RSR data files used:* 1 kHz bandwidth data: S10EAOE2005_123_0740NNNX43D.2A1 16 kHz bandwidth data: S10SROE2005123_0740NNNX43RD.2A2 *Supporting files for calibration and geometry calculations:* Reconstructed S/C trajectory: 050606R_SCPSE_05114_05132.bsp Planetary constants: cpck26Feb2009.tpc Leap seconds: naif0009.tls Earth station ephemeris: Earthstns_itrf93_050714.bsp Earth ephemeris: Earth_000101_090604_090313.bpc

Also plotted in the upper panel of Figure 3-10 is the difference between the reconstructed and predicted Doppler shifts, $f_{\text{dr}}(t) - f_{\text{dp}}(t)$, which accounts for the trend and a large fraction, but not all, of $f_{\text{offset}}(t)$. The difference, $f_{\text{resid}}(t) = f_{\text{offset}} - (f_{\text{dr}} - f_{\text{dp}})$, is the undulating curve plotted in the lower panel of Figure 3-10, here computed using coarser resolution to mitigate the effect of the noise on the frequency estimates. The most optically thick parts of Ring B still yield unreliable estimates (the green part of the plot). Least squares fit of the other more reliable parts of the curve (cyan color) yields the heuristic estimate $\hat{f}_{\text{resid}}(t)$. Potential causes for $\hat{f}_{\text{resid}}(t)$ could be persistent error in the reconstructed spacecraft trajectory and/or other un-modeled long-term effects. The upper panel of Figure 3-10 shows a comparison between the computed smooth estimate (solid red curve) $\hat{f}_{\text{offset}}(t) = \left[f_{\text{dr}}(t) - f_{\text{dp}}(t)\right] + \hat{f}_{\text{resid}}(t)$ with the measured (noisy green curve). The agreement is good.

The process described above is critical for ensuring that the phase of the calibrated signal $I_c(t) + iQ_c(t)$ is primarily due to the ring material, instabilities in the USO reference phase, and any other unknown short-time effects that are not possible to correct for.

3.3.4.2. **Power Calibration**

The second requirement for reliable computation of ring properties is accurate determination of the free-space signal level $P_0(t)$ used to normalize the signal level through the occultation period.

Direct measurement of $P_0(t)$ is possible only during time periods when the line-of-sight from the spacecraft to the Earth receiving station is clear of the rings. All ring occultation observations were designed to allow measurement of $P_0(t)$ over a sufficiently long period of time exterior to Ring A. The geometry of some radial occultations enabled measurements of $P_0(t)$ in the gap between Ring C and Saturn's ionosphere. When possible, measurements of $P_0(t)$ over known gaps within the rings were also used.

We use least squares spline fitting to obtain $P_0(t)$ estimates for the ring-free periods. The fitting yielded values $\hat{P}_0(t)$ everywhere throughout the observation period, as the example in Figure 3-11 illustrates. The calibrated, but still diffraction-limited, complex ring transmittance is defined as

$$\hat{T}_R(t) + i\hat{T}_I(t) = \left[I_c(t) + iQ_c(t)\right] / \sqrt{\hat{P}_0(t)} \tag{20}$$

The frequency-calibrated and normalized samples, $\hat{T}_R(t) + i\hat{T}_I(t)$, the *calibrated data*, provide the starting point for all subsequent data analysis steps including computation of optical depth profiles and scattered signal power spectra. The spectra shown in Figure 3-10 (BW =16 kHz data) were computed using calibrated data and standard power spectral estimation techniques (~2 seconds averaged spectra, each centered on the time listed in Figure 3-10).

As Figure 3-11 clearly shows, there are both short- and long-term variations in $P_0(t)$. The long-term variations are primarily caused by changes in the elevation angle of the DSN receiving antenna during the few to several hours of an experiment and systematic (spacecraft and/or ground) antenna pointing errors. The short-term fluctuations are typically caused by one or more terrestrial factors including turbulence in the atmosphere, clouds, wind gusts (causing mechanical vibration of the ground receiving antenna) or fluctuations in the receiver gain or thermal noise.

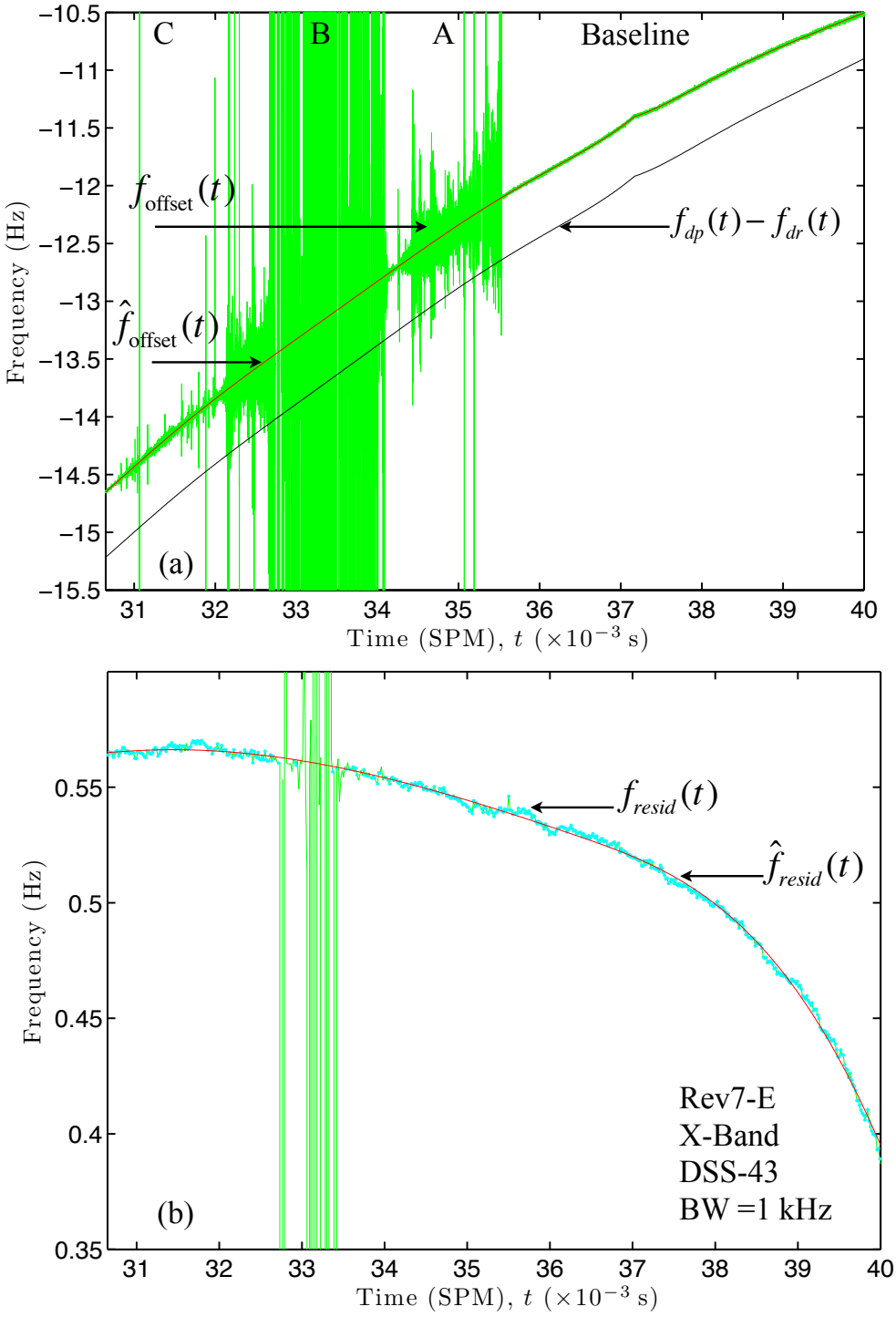

Figure 3-10: Example estimations of direct signal frequency offset (upper) and residual signal frequency (lower). SPM is seconds past midnight 2005-05-03.

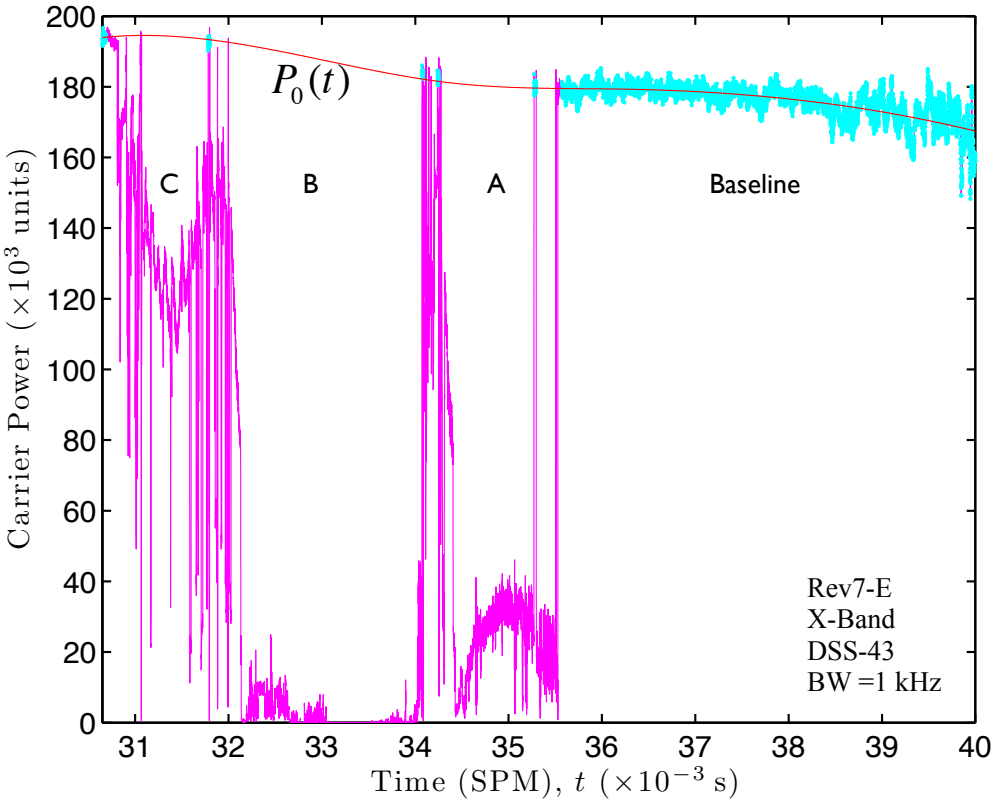

Figure 3-11: Example estimation of free-space signal power P_0(t). SPM is seconds past midnight 2005-05-03.

3.3.4.3. **Radial Interpolation**

Complex samples of the calibrated data are uniformly spaced in time. To translate the measurements to ring profiles, the reconstructed spacecraft trajectory is used to calculate the ring intercept radius as a function of time. The calculations are completed using a quasi-inertial Sun-centered reference frame with the light-time included. The procedures were developed for analysis of the Voyager ring occultation experiment and are documented in Rosen (1989). Ring radius accuracy better than few hundred meters is achievable in principle; the primary source of error is the orientation of Saturn's pole. The calculations here are based on the pole orientation in the planetary constants (PCK) files produced by the Cassini Navigation Team (see Table 3-2). The collective set of RSS (and other) occultations may, in turn, be used to improve future estimates of pole orientation and precession rate.

The velocity of the ring-plane intercept point varies radial. As a result, data sampled uniformly in time translate into samples that are non-uniformly spaced in ring radius. Any of several standard numerical interpolation algorithms may be used to interpolate the calibrated data onto a uniform radius grid. Care must be exercised, however, to ensure that interpolation errors are minimized. Below we use the notation

$$\hat{T}(\rho_0) = \hat{T}_R(\rho_0) + i\hat{T}_I(\rho_0) \tag{21}$$

to denote calibrated complex ring transmittance samples at radius ρ_0 where the sampling is uniform in radius. As described in detail in Marouf *et al*. (1986), $\hat{T}(\rho_0)$ provides the starting point for removing the diffraction effects and recover high-resolution profiles of ring optical depth. We provide a summary of the steps and an example below.

3.3.4.4. **Diffraction Correction**

Radio occultation observations of planetary rings are diffraction limited. The measured ring transmittance $\hat{T}(\rho_0)$, observed at time t and corresponding to a ring radius ρ_0, differs from the true value $\hat{T}(\rho_0)$, which would be observed just behind the ring plane, because of diffraction effects. The relationship is in the form of the Fresnel transform,

$$\hat{T}(\rho_0) = \frac{1-i}{2F}\int_{-\infty}^{\infty} T(\rho)\exp[i\frac{\pi}{2}(\frac{\rho_0-\rho}{F})^2]\,d\rho \tag{22}$$

where F is the Fresnel scale of diffraction, which depends on the observation wavelength and geometry (Marouf *et al*., 1986, Eq. 6). In principle, $T(\rho)$ may be recovered from $\hat{T}(\rho_0)$ by using the inverse Fresnel transform

$$T(\rho) = \frac{1+i}{2F}\int_{-\infty}^{\infty} \hat{T}(\rho_0)\exp[-i\frac{\pi}{2}(\frac{\rho-\rho_0}{F})^2]\,d\rho_0 \tag{23}$$

In practice quadratic phase approximations of the transform kernel (Marouf *et al*., 1986, Eqs. 15 and 16), sample resolution of $\hat{T}(\rho_0)$, and signal-to-noise in the measured values set limits on the $T(\rho)$ recovery.

The normal optical depth profile and the phase-shift profile are computed using the definitions

$$\tau(\rho) = -2\mu_0 \ln(|X(\rho)|) \tag{24}$$

$$\phi(\rho) = \tan^{-1}[X_I(\rho)/X_R(\rho)] \tag{25}$$

where we have used $\hat{X}(\rho_0) = \hat{T}(\rho_0) + \hat{n}(\rho_0)$ and $X(\rho) = T(\rho) + n(\rho) = X_R(\rho) + iX_I(\rho)$ to denote the noisy measured and recovered values, respectively, B is the ring opening angle, and $\mu_0 = \sin(|B|)$.

3.3.4.5. **Data Decimation and Profile Resolution**

Practical aspects of implementation of the Fresnel inversion procedure must be considered. Clearly, the infinite range of ρ_0 in (23) must be replaced by a finite data 'window' of width W, which sets a limit $\Delta R_W = 2F^2/W$ on the reconstructed resolution (Marouf *et al*., 1986). To preserve information about structure of spatial scale equal to or larger than some desired ΔR_W, the diffraction-limited data $\hat{T}(\rho_0)$ must be sampled at a rate equal to or

larger than twice the highest spatial frequency (in accordance with the sampling theorem). Thus, to resample $\hat{T}(\rho_0)$ at a reduced sampling rate, the data must first be low-pass filtered using a bandwidth commensurate with the lower sampling rate and then decimated so that the sample spacing is $\Delta R_W/2$ (or smaller) to prevent artifacts due to aliasing from corrupting the data.

Another potential source of corruption of the reconstructed ring profile is the artificial truncation of the data to finite width *W*. The sudden jump in the value of data samples near the window edge, from finite to zero value, introduces artifacts in the reconstructed $T(\rho)$ especially in optically think ring regions. The artifacts can be mitigated by multiplying the data by a tapered window function that gradually decreases to zero close to its edges (Marouf *et al*., 1986, Eq. 18). Parameters of the window function are chosen to minimize artifacts over the reconstruction dynamic range (optical depth range). Unfortunately, this is achieved at the cost of degradation in spatial resolution by a factor close to 2. The degraded resolution is usually referred to as the 'effective' resolution $\Delta R_{eff} = \sim 2\,\Delta R_W$; its initial value ΔR_W is referred to as the processing resolution.

Marouf *et al*. (1986) also discusses additional factors that limit achievable resolution, including uncertainty in knowledge of *F*, finite USO phase noise, and computational complexity of the inversion process.

An example of a diffraction reconstruction is shown in Figure 3-12 (Rev7-E occultation; see Table 3-2). The main ring feature shown is the Huygens Ringlet located within the Huygens Gap. Also shown is the so-called Charming Ringlet near the outer edge of the gap. The blue curves depict the diffraction-limited X-band profiles $\hat{\tau}(\rho_0)$ and $\hat{\phi}(\rho_0)$ at 250 m resolution. Edges of both ringlets as well as the outer gap edge are smoothed by diffraction; diffraction oscillations are visible in the vicinity of the Huygens Ringlet edges. The red curves depict the profiles $\tau(\rho)$ and $\phi(\rho)$ reconstructed using a processing resolution ΔR_W = 500 m, yielding profiles of effective resolution ΔR_{eff} close to 1 km.

3.3.4.6. **SNR-Resolution Tradeoff**

Note that the best achievable radial resolution for a given ring feature strongly depends on the optical depth of the feature, that is, on the measurement SNR. Finer spatial resolution requires data sampled at higher rate or, equivalently, data captured in a larger bandwidth, which are thereby noisier. Since the thermal noise is additive, the SNR can be improved using coherent averaging over a number of data samples, but at the expense of resolution.

There is always a tradeoff between finer resolution and uncertainty in the reconstructed profile that is analytically characterized by a parameter known as the threshold optical depth τ_{TH} , roughly the value of the ring normal optical depth for which the SNR drops to about 1. For a 70% confidence level, τ_{TH} is given by Marouf *et al*., (1986, Eqs. 23 to 26)

$$\tau_{TH} \cong -\mu_0 \ln[1.205 P_N] \tag{26}$$

where P_N is the average power of the additive noise in watts. An estimate $\hat{P}_N$ can be calculated from,

$$\hat{P}_N = \frac{1}{SNR_0}\frac{\dot{\rho}_0}{\Delta R} \qquad (27)$$

where ΔR is either $\Delta\rho_0$, the sample spacing of the diffraction-limited data, or ΔR_{eff}, the effective resolution of the reconstructed profiles; $\dot{\rho}_0$ is the ring plane radial velocity of the ring intercept point; and SNR_0 is the free-space SNR in 1 second integration time, or 1 Hz bandwidth. The latter can be estimated from the recorded I/Q samples. Alternatively, typical X-band values of about 54 and 48 dB-Hz for data collected at the 70- and 34-m ground stations, respectively, may be used.

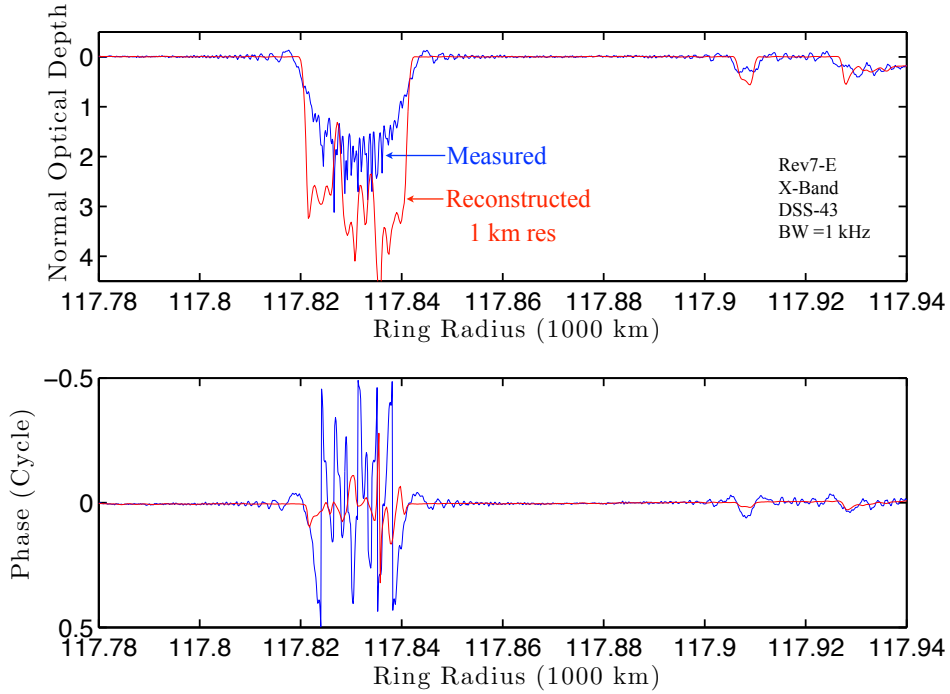

Figure 3-12: Optical depth and phase profile reconstructions from diffraction-limited Rev7-E ring occultation observations of 2005-05-03. The Huygens and 'Charming' Ringlets are at radii 117,830±11 km and 117,908±3 km, respectively. The outer edge of the Huygens Gap is at 117,927 km.

Figure 3-13 illustrates the tradeoff discussed above (again, Rev7-E, B = -23.5°, and $\dot{\rho}_0$ ~ 10 km/s; see Tables 3-1 and 3-2). The plots show the attenuation of the Titan Ringlet located within the Colombo Gap in inner Ring C at three progressively coarser resolutions of 100 m, 1 km, and 10 km. Also shown are the corresponding τ_{TH} levels - horizontal lines of the same color as the corresponding profile. The τ_{TH} levels progressively increase from ~3.1 to 4.0 to 5.0 as the resolution ΔR_{eff} changes from 100 m, to 1 km, to 10 km, respectively.

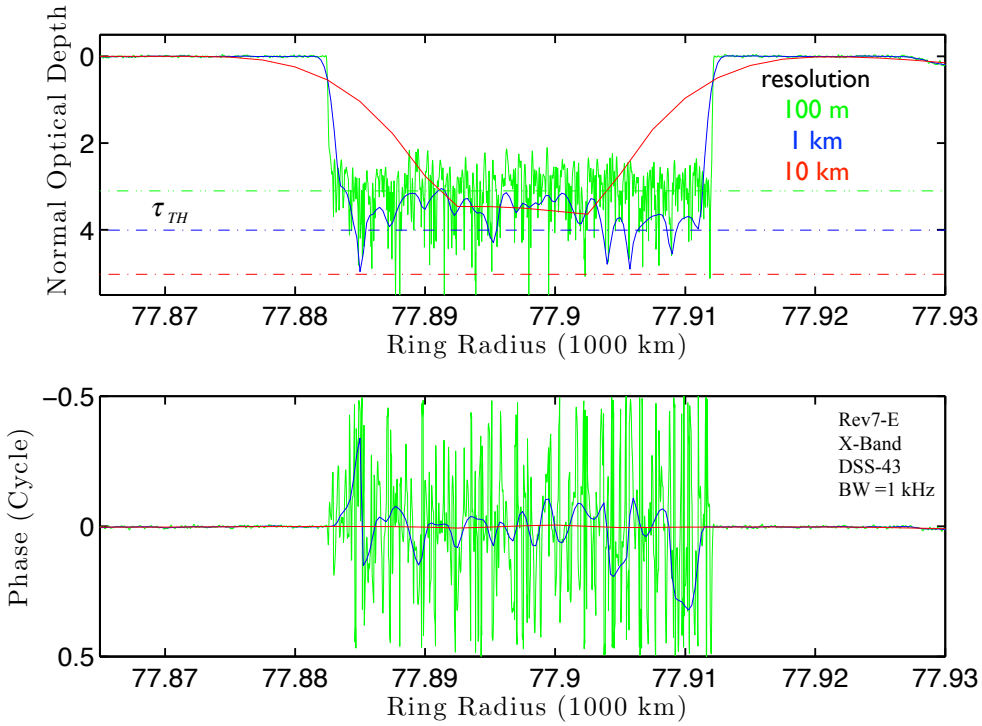

Figure 3-13: Example tradeoff between reconstruction resolution and measurement reliability for the Titan ringlet. The horizontal stippled lines identify the threshold optical depth (SNR ~ 1) for each indicated resolution.

At 100 m resolution (green profiles in Figure 3-13), almost all structure within the ringlet is obscured by noise; hence, the reconstruction is effectively noise limited and the phase profile is essentially random. The ringlet edge location is recovered with high accuracy, however. The absence of any profile overshoot in the vicinity of transition to a zero value free-space optical depth indicates reliable reconstruction of the diffraction effects.

At fine resolution, diffraction-limited data over a relatively large radial interval W is required to compute the inverse Fresnel transform. Any inaccuracies exceeding a small fraction of a cycle in the computed phase of the kernel of the inverse transform can cause undesirable artifacts in the reconstructed profiles.

At the 1 km resolution (blue profiles), more reliable profiling of ringlet structure is possible only over the fraction of its width where the recovered optical depth exceeds the corresponding threshold level (the horizontal blue line). The phase profile is also well behaved when $\tau < \tau_{TH}$. The edges remain relatively sharp at this resolution. At the coarsest 10 km resolution (red profiles), reliable measurement of an 'average' optical depth of the ringlet is achieved but the fine structure is lost — for example, the edges are highly smoothed. Relatively large threshold optical depths, such as the τ_{TH} ~5.0 here, are needed for profiling optically thick ring regions such as parts of Ring B.

3.4 rss_ringoccs – Open-Source RSS Ring Occultation Analysis Software

The RSS team has archived 1- and 10-km diffraction-recontstructed radial optical depth profiles of Saturn's rings on NASA's PDS Ring-Moon Systems Node, for X-band observations from Rev 7 (in 2005) to Rev 67 (in 2008). A more comprehensive set of 1- and 10-km profiles for S-, X-, and Ka-band observations up to the time of the USO failure has been peer-reviewed, and is expected to be publicly available on the PDS by the end of 2018. These results were obtained under the direction of RSS team member Essam Marouf, and represent the state-of-the-art in signal processing and diffraction reconstruction.

As part of the Cassini mission closeout, the Project Scientist directed all ring occultation instruments (VIMS, UVIS, and RSS) to provide calibrated radial ring profiles at the highest achievable resolution. In response to this charge, members of the RSS team under the direction of RSS team leader Richard French developed a completely independent end-to-end open-source occultation analysis package to enable the general user community to produce diffraction-reconstructed ring profiles at any desired resolution, limited by SNR, the sampling theorem, and ring occultation geometry. This Unix-based Python 3 software package – dubbed rss_ringoccs – is hosted on Github at https://github.com/NASA-Planetary-Science/rss_ringoccs.

The purpose of rss_ringoccs is to enable scientists to produce "on demand" radial optical depth profiles of Saturn's rings from the raw RSS data, without requiring a deep familiarity with the complex processing steps involved in calibrating the data and accounting for the effects of diffraction. The code and algorithms are extensively documented, providing a starting point for users who wish to to test, refine, or optimize the straightforward methods we have employed. The emphasis has been on clarity, sometimes at the expense of programming efficiency and execution time. rss_ringoccs does an excellent job of reproducing existing RSS processed ring occultation data already present on NASA's PDS Ring-Moons Node, but we make no claim to having achieved the state-of-the-art in every respect. We encourage users to augment our algorithms and to report on those improvements, so that they can be incorporated in future editions of rss_ringoccs.

3.5 Surface Scattering

Bistatic radar (BSR) is the active probing of planetary surfaces by oblique reflection and scattering of microwave signals. Such observations provide statistical information on root-mean-square (rms) surface slopes and on dielectric constant and density at scales comparable to the radio wavelength (centimeters to meters). An unmodulated radio signal, transmitted from the spacecraft, is scattered by the surface, and the echo is received at a ground station on Earth. A direct signal (from the spacecraft) is often received at the same time, providing a frequency reference for the echo. Fjeldbo (1964) utilized physical optics theory to explain the specular component of the echo as an aggregation of mirror-like reflections from properly oriented elements of the undulating surface. For typical spacecraft transmitters of 1-100 watts, surface echoes as small as 1 zeptowatt (10^{-21} W) can be detected. BSR experiments have been carried out on the Moon, Venus, Mars, and Titan using Soviet, U.S., and European spacecraft (Simpson, 2007).

Differential Doppler effects between the direct and reflected paths separates the received echo from the carrier. Dispersion of the echo itself, caused by differential Doppler within the reflecting region, provides a measure of the rms slope of the undulations. Where echo dispersion is not large, the Doppler difference between the two primary paths can be used to infer large-scale topography of the surface. An incident signal with known polarization will generate a reflected signal with both the original and orthogonal components; application of Fresnel reflection theory to absolutely calibrated echoes in one polarization or to relatively calibrated echoes in orthogonal pairs can be used to recover the dielectric constant of the surface material. A simple model relating dielectric constant to porosity then allows estimation of material density.

The quantities of interest in BSR are the amplitude, frequency, and polarization as well as the time of the echo signal. Incremental echo power from an unresolved surface element is given by the radar equation:

$$dP_R = (P_T G_T / 4\pi R_T^2)\ \sigma (A_R / 4\pi R_R^2) \tag{28}$$

where P_T is the transmitted power, G_T is the transmitting antenna gain in the direction of the surface element, R_T is the distance from the transmitter to the surface element, A_R is the effective area of the receiving antenna aperture, and R_R is the distance from the surface element to the receiver. The bistatic radar cross section of the surface element, σ, is

$$\sigma = \int \sigma_0\, dS \tag{29}$$

where dS the area of the surface element and σ_0 is the specific radar cross section, or radar cross section per unit area, which is a function of the directions of both the incoming and outgoing wave vectors. For quasi-specular conditions, these reduce to a single angle $\phi = \phi_i = \phi_r$ measured with respect to the local mean surface. Specific radar cross section is assumed to be proportional to reflectivity, ρ, which is derived from the Fresnel voltage reflection coefficients for horizontally and vertically polarized electromagnetic waves at a planar interface between free space and the planetary surface. So

$$R_{HH} = (\cos\phi - (\varepsilon - \sin^2\phi)^{1/2}) / (\cos\phi + (\varepsilon - \sin^2\phi)^{1/2}) \tag{30}$$

$$R_{VV} = (\varepsilon\cos\phi - (\varepsilon - \sin^2\phi)^{1/2}) / (\varepsilon\cos\phi + (\varepsilon - \sin^2\phi)^{1/2}) \tag{31}$$

where ε is the dielectric constant of the surface material. The reflection coefficients for circularly polarized waves can be derived from R_{HH} and R_{VV}

$$R_{SC} = (R_{VV} + R_{HH})/2 \tag{32}$$

$$R_{OC} = (R_{VV} - R_{HH})/2 \tag{33}$$

where R_{SC} is the voltage reflection coefficient for same sense circular polarization, *e.g.*, right-hand circular polarization (RCP) transmitted and RCP received, and R_{OC} is the coefficient for the opposite sense, *e.g.*, RCP transmitted and left-hand circular polarization (LCP), received.

The power reflection coefficients r_i are:

$$r_{SC} = |R_{SC}|^2 \text{ and } r_{OC} = |R_{OC}|^2 \quad (34)$$

The ratio ρ_{SC}/ρ_{OC} is sometimes easier to measure than either component by itself because many terms in (28) are common to both signal paths (Simpson, 2007).

The Doppler shift for a spacecraft transmitter at $\boldsymbol{r}_T$ and receiver at $\boldsymbol{r}_R$ is the rate of change of the path length measured in wavelengths λ (Figure 3-14)

$$f_c = (d/dt) \mid \boldsymbol{r}_R - \boldsymbol{r}_T \mid /\lambda \quad (35)$$

The vectors must be defined in an inertial frame and light time adjustments must be included but are not shown explicitly. The Doppler shift for a signal reflected by the specular point $\boldsymbol{r}_P$ on a smooth target is, similarly

$$f_e = (d/dt) \mid \boldsymbol{r}_R - \boldsymbol{r}_P \mid /\lambda \;\; (d/dt) \mid \boldsymbol{r}_P - \boldsymbol{r}_T \mid /\lambda \quad (36)$$

For a surface on which the roughness is not too severe, the total echo power is the same as the power from the single specular point on the equivalent perfectly smooth sphere. As roughness increases, the spatial distribution of the reflecting facets becomes broad enough that some of the glints fall outside the illumination pattern of the spacecraft antenna, and the observed echo power is reduced accordingly. In the extreme case, only a small fraction of the possible glints are illuminated, and the distribution of incremental echo power reflects the antenna pattern rather than the surface scattering function. Broader echoes result from rougher surfaces and/or more rapidly moving spacecraft. For experiments that are not 'beam limited,' the half power width of the echo B and the rms roughness of the surface ζ are related to V, the velocity of the specular point across the surface by:

$$B = 4 (\ln 2)^{1/2} (V/\lambda)\cos\phi \quad (37)$$

The Cassini RSS team carried out a number of bistatic experiments near the Brewster angle at Titan to determine reflectivity and dielectric constant estimates at its three radio wavelengths (Table 3-3).

Table 3-3
Cassini Bistatic Radar Experiments

Start Date	Data Set	Target
2006-03-18	CO-SSA-RSS-1-TBOC1-V1.0	Titan
2006-05-20	CO-SSA-RSS-1-TBOC2-V1.0	Titan
2007-03-25	CO-SSA-RSS-1-TBOC3-V1.0	Titan
2007-07-18	CO-SSA-RSS-1-TBIS1-V1.0	Titan
2008-11-03	CO-SSA-RSS-1-TBOC4-V1.0	Titan
2009-03-27	CO-SSA-RSS-1-TBIS2-V1.0	Titan
2009-04-04	CO-SSA-RSS-1-TBOC5-V1.0	Titan

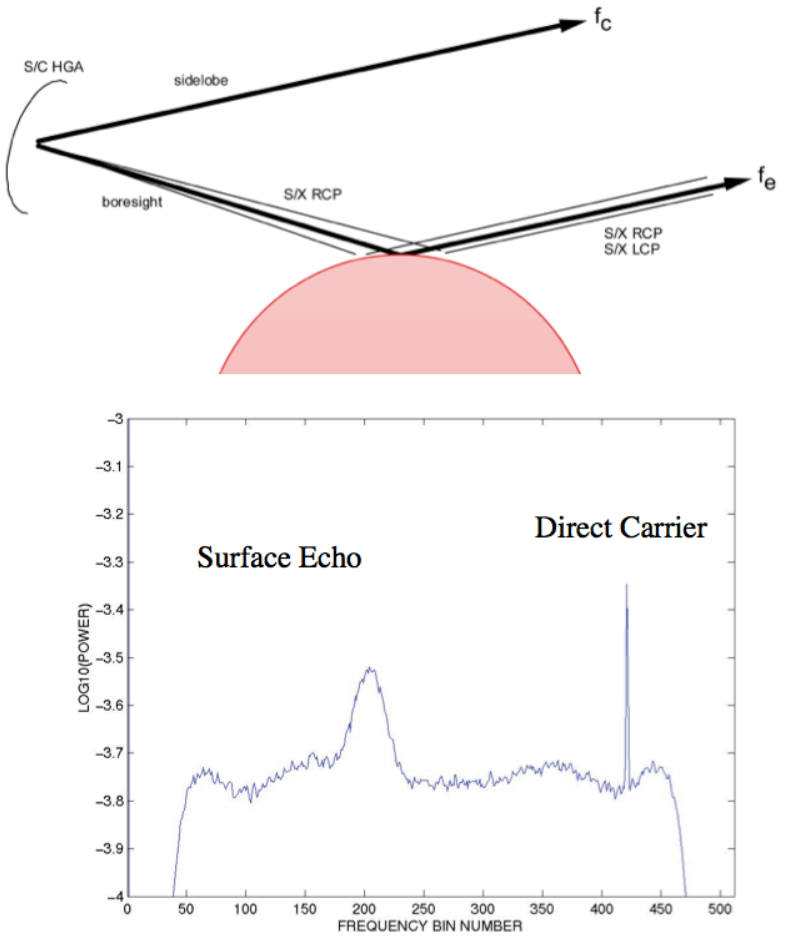

Figure 3-14: Representation of a bistatic radar experiment and resulting spectrum. The directly propagating signal is at frequency bin ~420; the surface echo extends over bins ~175-230.

3.5.1 Titan Surface Scattering Results

The first Cassini detectable X-band RS bistatic echoes from Titan's surface were observed on flyby T14 on May 20, 2006 (DOY 140), making Titan the most distant solar system object for which bistatic echoes were successfully detected. The echoes were weak but clearly detectable. Right circularly polarized sinusoidal signal was transmitted by Cassini and both the right and left circularly polarized (RCP and LCP) surface reflected components were observed at the 70-m station of the DSN at Madrid, Spain (DSS-63).

Cassini was maneuvered continuously to track the region of Titan's surface where mirror-like (quasi-specular) reflected signals may be observed. The ground receivers were tuned to compensate for the large Doppler shift due to relative spacecraft-Titan-Earth motion, allowing detection of the echoes near the center of the recording bandwidth (Figure 3-14 and 3-15).

The experiment was designed to probe incidence angles θ close to the Brewster, or polarization, angle of likely surface compositions. Careful measurements of the system noise temperature allowed determination of the absolute power in each polarized echo component and hence their ratio. The polarization ratio, the known observation geometry, and Fresnel reflectivity were then used to determine the dielectric constant ε.

The T14 surface echoes were detectable on both the inbound and outbound sides, but were intermittent along the ground tracks, suggesting mostly rough terrain occasionally interrupted by patches of relatively flat areas. Polarization ratio measurements were obtained for two localized surface regions of similar latitude ~15°S, well separated longitudes ~14 and ~140° W, and incidence angle θ ~56° and ~64°, respectively. For both regions, the measurements implied surface dielectric constant $\varepsilon \sim 1.6$, suggesting liquid hydrocarbons, although alternative interpretations are possible (Marouf et al., 2006 Fall AGU, P11A- 07; Marouf et al., 2008 Fall AGU, P21A-1319).

In Figure 3-14, panels (a) and (b) depict selected geometry parameters of the Cassini T14 bistatic scattering observations. The parameters are plotted versus time relative to closest approach. Inbound (blue) and outbound (red) bistatic observations were implemented before and after the T14 ionospheric/atmospheric occultation (the empty gap in both panels). Panel (c) depicts the corresponding ground tracks. The Huygens Probe landing site is shown for reference purposes. The polarization ratio measurements were obtained for two localized surface regions of similar latitude ~15°S, well separated longitudes ~14 and ~140° W, and incidence angle θ ~56° and ~64°, respectively.

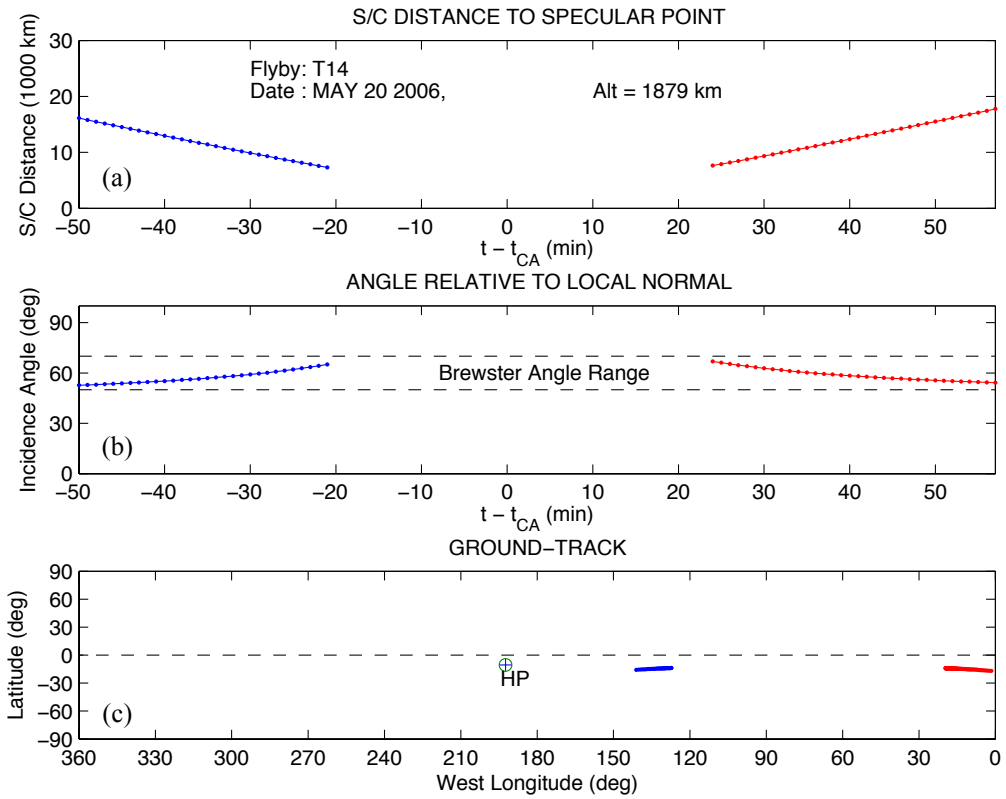

Figure 3-14: Panels (a) and (b) depict selected geometry parameters of the Cassini T14 observations and panel (c) depicts the corresponding ground tracks. The Huygens Probe landing site is shown for reference purposes.

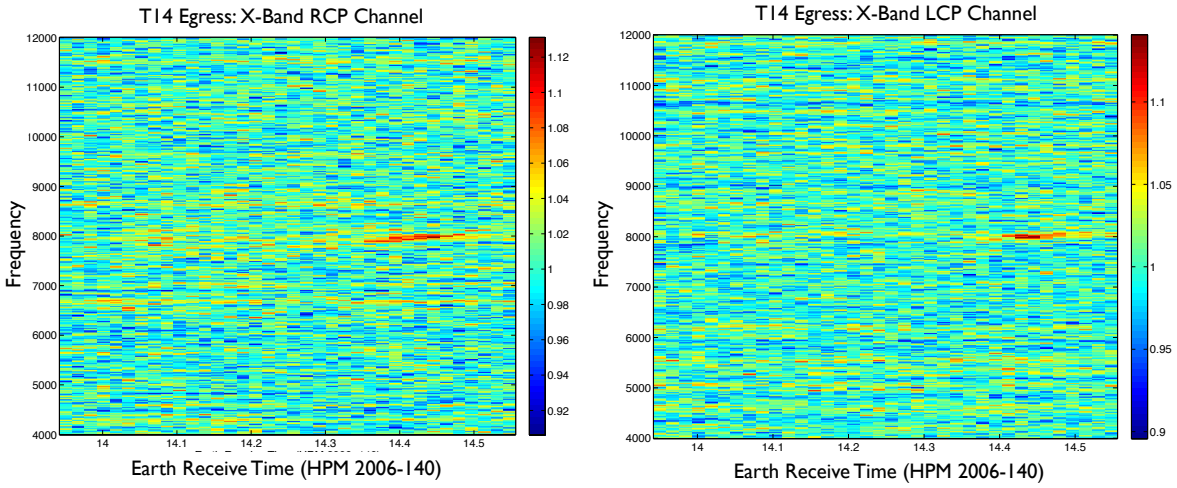

Figure 3-15: Uncalibrated spectrograms of the first positive detection of bistatic echoes from Titan surface observed on the T14 flyby on May 20, 2006 (DOY 140). The weak echoes were simultaneously detectable in both the RCP and LCP 16 kHz bandwidth X-band channels of the 70-m ground station of the Madrid, Spain, DSN complex (DSS-63).

3.6 Fundamental Physics

3.6.1 Search for Low-Frequency Gravitational Radiation

Gravitational waves (GWs) are propagating, polarized gravitational fields – 'ripples' in the curvature of space-time (Thorne, 1987). Such waves are predicted by all relativistic theories of gravity although different theories of gravity predict different properties of the radiation, *e.g.*, propagation states and propagation speed. These waves are propagating space-time strain, so their amplitudes are dimensionless strain amplitudes. These waves cause fractional frequency shifts of electromagnetic waves exchanged between separated test mass and cause differences in the rates at which separated clocks keep time.

In General Relativity, GWs are propagating solutions of the Einstein field equations, waves that carry energy and momentum and, like electromagnetic waves, are transverse to the propagation direction, have two independent polarization states, and propagate at the speed of light. However, unlike electromagnetic waves, gravitational waves couple very weakly to matter. Gravitational waves are generated at potentially detectable levels only by very massive sources undergoing extreme dynamics. Because of their weak interaction, GWs propagate unchanged from their sources, essentially unaffected by scattering or absorption by intervening matter. Hence GWs preserve information about the deep interiors of high gravity, high velocity objects. GWs provide a direct strong-field test of fundamental physics and provide a new window for observational astronomy with information fundamentally different from that available with electromagnetic observations.

The Doppler tracking technique uses the Earth and a distant spacecraft as separated free test masses with the ground-based Doppler tracking system continuously measuring the Earth-spacecraft fractional Doppler shift

$$y = \delta f / f_0 \tag{38}$$

where δf is the Doppler shift and f_0 is the radio link's carrier frequency. Unlike other GW detectors, the ~1-10 AU Earth-spacecraft separation makes the detector large compared with ~millihertz-frequency gravitational wavelengths. Consequently times-of-flight of the GWs and radio waves through the apparatus are important and impose characteristic signatures of GWs in the observed Doppler time series.

The Cassini gravitational wave experiment consisted of 3 campaigns:

- GWE1 (2001 DOY 330 – 2002 DOY 004)
- GWE2 (2002 DOY 339 – 2003 DOY 014)
- GWE3 (2003 DOY 314 – 2003 DOY 332).

3.6.1.1 Observables

The raw data are the pre-detection outputs from one or more RSRs, as described above. These data consist of samples of the electric field in a specific radio polarization, taken as in-phase and quadrature (I/Q) samples at a rate of 1000 I/Q pairs per second. Data were

always taken at X-band (X uplink and X-downlink); at DSS25 data were also taken at Ka-band (X-uplink, Ka-band downlink) and – for GWE1 and GWE2 only – with Ka-band uplink and Ka-band downlink.

3.6.1.2 **Analysis**

3.6.1.2.1 **Data Samples and RSR Output Frequency**

Data samples and RSR output frequency, as well as the steps to convert to the sky frequency are described in section 2.3.2.1.

3.6.1.2.2 **Media Calibration**

Two important sources of noise are frequency fluctuations imposed on the radio wave as it traverses irregularities in the solar wind and Earth's ionospheric plasma and as it traverses irregularities in the Earth's neutral atmosphere. For DSS-25 observations in GWE1 and GWE2 there is sufficient information to solve for and remove the plasma noise within the geometric optics approximation (see Bertotti *et al*. (2003) and references therein). Boresighted water vapor radiometry data were taken with the AWVR. The AWVR data give estimates of the downlink tropospheric path delay. Since tropospheric noise enters with a transfer function of $\delta(t) + \delta(t + T_2)$, where T_2 is the two-way light time between the station and the spacecraft, the tropospheric effect can be suppressed by applying this correction (see, *e.g.*, Armstrong (2006) for a discussion of the noise budget).

3.6.1.2.3 **Residuals**

The average Doppler shifts due to Earth and spacecraft motion must be removed. The Orbit Determination Program (ODP) can be used, and is preferred for precision work or for searches to very low frequency parts of the band (~microhertz.) The difference between the observed sky frequency and the predicted sky frequency after taking all known effects into consideration is the residual frequency; when divided by the link center frequency, f_0, it gives the time series of fractional frequency fluctuations, y(t), which are the scientific data needed to search for GWs.

3.6.1.2.4 **Detection**

The GW signature in the time series is (Estabrook and Wahlquist 1975; Armstrong 2006 equations 1 and 2):

$$y_{signal} = ((\mu-1)/2)\, Y(t) - \mu Y(t - ((1+\mu)/2)^* T_2) + ((1+\mu)/2)^* Y(t - T_2), \quad (39)$$

where μ is the cosine of the angle between the Earth-spacecraft line and the propagation vector for the GW, $Y(t) = (n \cdot h \cdot n)/(1 - \mu^2)$, and n is a unit vector from the Earth to the spacecraft; **h**(t) is the first order metric perturbation at the earth. This 'three pulse' response of the Doppler to a GW excitation is interpreted as due to the GW striking the Earth, the

GW striking the spacecraft (at a delayed time) and the original Earth buffeting transponded back to the Earth a two-way light time later.

3.6.1.2.5 **Noise**

Noise competes with the GW signal in the detection process. A thorough discussion of noise sources, their transfer functions, and their mitigation for the GW experiment is given in Asmar *et al*. (2005). Example plots of some of the noise sources and their transfer functions are given in Armstrong (2006). A discussion of the error budget of the Doppler signal is given in Section 4 of Armstrong (2006).

3.6.2 **Precision Tests of Relativistic Gravity**

3.6.2.1 **Parameterized Post-Newtonian (PPN) Representation**

The Parameterized Post Newtonian (PPN) formalism is a formal approach to compare metric theories of relativistic gravity with each other and with experiments. The PPN approach is simplest in the slow motion, weak field limit appropriate for solar system tests of relativistic gravity. ('Slow motion' means $v^2/c^2 << 1$, where v is a velocity relative to the solar system barycenter, and 'weak field' means |Newtonian potential|$/c^2 << 1$. In the inner solar system $|v| \sim 30$ km/sec so $v^2/c^2 \sim 10^{-8}$. At the surface of the Sun, $G M_{Sun}/r_{Sun} \approx 2\times10^{11}$ m^2/s^2, so that |Newtonian potential|$/c^2$ is less than or of order 10^{-6} everywhere in the accessible solar system).

There are 10 PPN parameters (Tables 2 and 4 of Will (2006)) used in the classification of theories and in comparing those theories with observations. RS experiments have principally been concerned with PPN parameter γ and with constraints to a possible time variation of the Newtonian gravitational 'constant'. Heuristically, PPN γ characterizes space-time curvature produced per unit mass. PPN parameters take on different values in different theories of relativistic gravity; for General Relativity (GR), $\gamma = 1$.

3.6.2.2 **Determinations of PPN γ with the Cassini Spacecraft**

As described in Iess and Asmar (2006), RS determinations of γ have been based on measurements of the range and range rate between Earth and a distant spacecraft as the line-of-sight passes close to the Sun (Bertotti *et al.* 2003). A radio signal sent between the Earth and a spacecraft has an additional non-Newtonian contribution to the range due to space-time curvature caused by the Sun's mass. Expressed as time-delay, this relativistic contribution to the observed one-way range is approximately (Will 2006):

$$\Delta t \approx ((1 + \gamma)/2) (240 - 20 \ln((b/r_{Sun})^2/(r/1\ AU))) \text{ microseconds} \qquad (40)$$

where b is the impact parameter of the ray (closest approach to the Sun), r_{Sun} is the solar radius, and r is the range to the spacecraft.

The classical RS method of estimating γ is to fit ranging data to the logarithmic part of (42) as the spacecraft passes through solar conjunction. γ was measured to be unity (*i.e.*, the GR value) to about 1 part in 1000 based on Viking ranging observations in the 1970s.

In a significant departure from the Viking experiment, Cassini did not measure the travel time of photons to and from the spacecraft, but rather exploited precision measurements of the spacecraft radial velocity. The radial velocity (more precisely, the two-way range rate) is obtained by measuring the phase of the received carrier. Phase measurements are extremely accurate, due to the use of highly stable frequency standards both in the generation of the uplink signal and in the detection of the received phase. The ground and spacecraft electronics are carefully designed to preserve the phase coherence of the radio link, a characteristic particularly important for spacecraft transponders used in the onboard reception of the carrier and its retransmission to ground. Although Cassini supported range measurements accurate to 1-2 m in the X-band channel, ranging data are far less useful than direct range rate measurements for the detection of the relativistic effect.

Due to the motions of the spacecraft and the Earth during the conjunction, the closest approach distance changes with time, inducing a relative frequency shift of the carrier approximately equal to

$$\frac{\Delta\nu}{\nu} = -\frac{d\Delta t}{dt} \cong -4(1+\gamma)\frac{GM}{bc^3}\frac{db}{dt} = -(20\,\mu\text{s})(1+\gamma)\frac{1}{b}\frac{db}{dt} \tag{41}$$

In 2002, the Cassini spacecraft was at a heliocentric distance of 7.4 AU, en route to Saturn. The quantity db/dt is therefore very close to being determined by the Earth orbital velocity and the relative frequency shift was of order 10^{-10} to 10^{-9} depending on the distance of the radio beam from the Sun. This quantity is almost five orders of magnitude larger than the measurement noise of the Cassini radio system.

All observations of propagating radio signals are strongly affected by the solar corona, turbulent plasma that causes random variations in the optical path. Since the refractive index of the coronal plasma in the microwave region of the spectrum is inversely proportional to the square of the carrier frequency, the Cassini experiment exploited its multi-frequency radio links at X and Ka-bands for a nearly complete cancellation of the plasma effects (Bertotti *et al*. 1993). This immunity to plasma noise was crucial for the experiment's success.

A crucial component of the plasma noise cancellation system was a novel Ka-band radio link especially developed for Cassini radio science experiments (in particular for the gravitational wave experiment — carried out during the cruise phase — but also for the determination of the gravity fields of Saturn and its satellites). The 34 m station DSS-25, located at the Goldstone DSN complex, underwent significant upgrades, including installation of an improved frequency and timing system, installation of a precision Ka-band transmitter, a tropospheric scintillation correction system, and a monopulse pointing system. Of particular relevance was the separation of the transmitting and receiving feeds, required to account for aberration effects. Indeed, for observations at some times of the year the angular

separation between the arrival direction of the spacecraft signal from the direction of the transmitted beam is comparable to or larger than the half-power beam-width of the ground antenna at Ka-band. The separation reaches its largest value near solar conjunction, when the apparent transverse velocity of the spacecraft seen from Earth is maximum.

The key onboard device is a Ka-band frequency translator, whose main functional requirement is the coherent retransmission to ground of the received uplink Ka-band signal. This unit, provided by ASI, was especially designed for high phase stability. According to its specifications, the relative frequency shift introduced by the translator (measured in terms of Allan deviation) could not exceed 4×10^{-16} over time scales of 1000 s, a figure confirmed by ground tests. At this level of stability, the unit does not affect in any appreciable way the end-to-end frequency stability of the radio link. In general, onboard and ground electronics, including the frequency standard, are not a significant error source in Cassini Doppler measurements.

The error budget of the Cassini conjunction experiment was dominated by two nearly equally error sources: propagation effects in the Earth's troposphere and mechanical and thermal deformations of the ground antenna. While no special attempt was made to increase the antenna thermo-mechanical stability, dedicated instrumentation was developed for calibration of the tropospheric effects (Keihm 1995). The AMC system (Keihm *et al*., 2004) consists of a very precise water vapor radiometer, a microwave temperature profiler and a sensitive digital barometer, capable of measuring the tropospheric relative frequency shift under summer conditions with a precision of $5\text{-}10 \times 10^{-15}$. The AMC proved particularly important during the Cassini conjunction experiment, allowing reduction of the residual noise after plasma compensation by a factor of about three. The final Allan deviation of the frequency residuals at 1000 s integration time was 1.5×10^{-14}, nearly constant independent of the solar elongation angle, with the only exception being a pass a day past conjunction when the X-band radio links were affected by strong amplitude fluctuations. A detailed analysis of the error budget was carried out by Asmar *et al.* (2005).

Doppler data acquired with the ground antenna DSS25 in 18 passes from 6 June to 7 July 2002 were used in the data analysis. Range data, available only from the X-band radio link, were intrinsically less accurate and strongly affected by solar plasma; therefore they were not included in the analysis. The conjunction occurred on June 21, 2002, with a minimum impact parameter of 1.6 solar radii, and no occultation. Throughout the experiment the spacecraft remained in a quiet dynamical and thermal state. Thanks also to the large distance of the spacecraft from the Sun (7.4 AU) and all planets, the dynamical model used in the trajectory fit was particularly simple. The only forces whose uncertainty could have detectable effects in the Doppler data were the solar radiation pressure and the anisotropic thermal emission from the three RTGs. The corresponding non-gravitational accelerations were small due to the large mass of the spacecraft (5200 kg). The RTG thermal thrust is constant in the spacecraft frame (whose inertial orientation is accurately known) and can therefore be easily modeled by introducing three unknown, solve-for parameters in the dynamical model.

The largest component of the acceleration, oriented along the axis of the high gain antenna, has been estimated at a value of 3×10^{-9} m/s^2. The solar radiation pressure (6.4×10^{-11} m/s^2, significantly smaller than the RTG-induced acceleration due to the large heliocentric distance) was due almost entirely to the 4 m high gain antenna. The small and slowly varying solar aspect angle induces only a slight and easily modeled variation during the experiment. The main uncertainty results from the poor knowledge of the antenna specular and diffuse reflectivity, subject to variations after the exposure to the space environment. These quantities are assumed to be constant throughout the experiment.

A total of twelve quantities were used in the orbital fit — the six components of the spacecraft state vector at a reference epoch, the three components of the RTG-induced acceleration, the specular and diffuse reflectivity of the spacecraft high gain antenna, and the PPN parameter γ. Remarkably, the determination of the spacecraft position was very accurate, with formal errors of 3.5 km, 46 km and 35 km along the three axes of the J2000 frame. This result, obtained during the cruise phase, from Doppler data only, and across a solar conjunction has no precedent in interplanetary navigation (Tortora *et al*., 2004).

4. References

820-013, Deep Space Mission System (DSMS) External Interface Specification:, JPL D-16765 (internal document available to flight projects).

Anderson, J. D., and M. R. Warner, 1966: Determination of the masses of the moon and Venus, and the astronomical unit from radio tracking of Mariner II. In *Trajectories of Artificial Celestial Bodies*, pp. 216-246, Springer-Verlag, New York.

Anderson, J. D., 1974: Geodetic and dynamical properties of planets. EOS, Vol. 5, 515-523.

Armstrong, J. W. 2006: Low-frequency gravitational wave searches using spacecraft Doppler tracking *Living Reviews in Relativity*, 9 (2006), 1. [Online Article] January 24, 2006, http://www.livingreviews.org/lrr-2006-1

Asmar, S. W., J. W. Armstrong, L. Iess, and P. Tortora, 2005: Spacecraft Doppler tracking: noise budget and achievable accuracy in precision radio science observations, *Radio Science 40,* RS2001, doi:10.1029/2004RS003101

Asmar, Sami, 2010: Radio as a science tool, *Proceedings of the IEEE* , Issue 10, 1686-1687doi 10.1109/ JPROC.2010.2060247

Asmar, Sami, Kaare Aksnes, Roberto Ambrosini, Aseel Anabtawi, John D. Anderson, John W. Armstrong, David Atkinson, Jean-Pierre Barriot, Bruno Bertotti, Bruce G. Bills, Michael Bird, Veronique Dehant, Peter Edenhofer, F. Michael Flasar, William Folkner, Richard G. French, Hideo Hanada, Bernd Häusler, David P. Hinson, Luciano Iess, Özgür Karatekin, Arvydas J. Kliore, Alex S. Konopliv, Frank Lemoine, Ivan Linscott, Essam Marouf, Jean-Charles Marty, Koji Matsumoto, Hirotomo Noda, Kamal Oudrhiri, Meegyeong Paik, Ryan S. Park, Martin Pätzold, Robert Preston, Nicole Rappaport, Pascal Rosenblatt, Richard A. Simpson, David E. Smith, Suzanne Smrekar, Paul G. Steffes, Silvia Tellmann, Paolo Tortora, G. Leonard Tyler, Tim Van Hoolst, Michael Watkins, James G. Williams, Paul Withers, Xiaoping Wu, Donald Yeomans, Dah-Ning Yuan, Maria T. Zuber, 2009a: Planetary radio science: Investigations of interiors, surfaces, atmospheres, rings, and environments. A White Paper submitted to the 2009 Planetary Sciences Decadal Survey

Asmar, Sami, John W. Armstrong, Neil Ashby, Peter Bender, Bruno Bertotti, William M. Folkner, Luciano Iess, Andrea Milani, Robert Preston, Paolo Tortora, Slava G. Turyshev, James G. Williams, Xiaoping Wu, 2009b: Radio science techniques for solar system tests of general relativity, A White Paper submitted to the Fundamental Physical Sciences Panel of the 2009 Decadal Survey

Asmar, Sami W., Alexander S. Konopliv, Michael M. Watkins, James G. Williams, Ryan S. Park, Gerhard Kruizinga, Meegyeong Paik, Dah-Ning Yuan, Eugene Fahnestock, Dmitry Strekalov, Nate Harvey, Wenwen Lu, Daniel Kahan, Kamal Oudrhiri, David

E. Smith, Maria T. Zuber, 2013: The scientific measurement system of the gravity recovery and interior laboratory (GRAIL) Mission, *Space Science Reviews* 178, 25—55, DOI 10.1007/s11214-013-9962-0.

Bender, E., 1973. An equation of state for predicting vapour–liquid equilibria of the system N_2–Ar–O_2. *Cryogenics* 13, 11–18.

Bertotti, B., Comoretto, G. & Iess, L. 1993: Doppler tracking of spacecraft with multifrequency links. *Astron. Astrophys*. 269, 608–616.

Bertotti, B., Iess, L., and Tortora, P., 2003: A test of general relativity using radio links with the Cassini spacecraft, *Nature*, *425*, 374-376.

Bird, M. K. et al. 1992: ULYSSES radio occultation observations of the Io plasma torus during the Jupiter encounter, *Science* 257, 1531-1535.

Eshleman, V.R., G. Fjeldbo, J.D. Anderson, A. Kliore, and R.B. Dyce, 1968: Venus: lower atmosphere not measured, *Science* 162, 661- 665.

Eshleman, V.R., G.L. Tyler, J.D. Anderson, G. Fjeldbo, G.S. Wood and T.A. Croft, 1977: Radio science investigations with Voyager, *Space Science Reviews* 21, 207-232.

Estabrook, F. B. and Wahlquist, H. D., 1975: Response of Doppler spacecraft tracking to gravitational radiation, *Gen. Rel. Grav.* 6, 439-447.

Fjeldbo, G., 1964: Bistatic Radar Methods for Studying Planetary Ionospheres and Surfaces, SU-64-025, Stanford Electronics Laboratories, Stanford, California.

Fjeldbo, G., and V.R. Eshleman, 1968: The atmosphere of Mars analyzed by integral inversion of Mariner IV occultation data, *Planet Space Science* 16, 1035-1059.

Fjeldbo, G., A.J. Kliore, and V.R. Eshleman, 1971:The neutral atmosphere of Venus as studied with the Mariner V radio occultation experiments, *The Astronomical Journal* 76, 123-140.

Howard, H.T., V.R. Eshleman, D.P. Hinson, A.J. Kliore, G.F. Lindal, R. Woo, M.K. Bird, H. Volland, P. Edenhofer, M. Pätzold, H. Porsche, 1992: Galileo radio science investigations, *Space Science Reviews* 60, 565-590.

Iess, Luciano, Nicole Rappaport, Robert Jacobson, Paolo Racioppa, David Stevenson, Paolo Tortora, John Armstrong, Sami Asmar, 2010: Gravity field, shape and moment of inertia of Titan, *Science* 327, 1367-1369, 10.1126/science.1182583.

Iess, Luciano, Robert Jacobson, Marco Ducci, David Stevenson, Jonathan Lunine, John Armstrong, Sami Asmar, Paolo Racioppa, Nicole Rappaport, Paolo Tortora, 2012: The tides of Titan, *Science* 337, 457-459, 10.1126/science.1219631.

W.M. Kaula, 1966: *Theory of Satellite Geodesy*. Blaisdell, Waltham.

Keihm, S. J., 1995: Water vapor radiometer measurements of the tropospheric delay fluctuations at Goldstone over a full year, *TDA Progress Report*, *42-122*, 1-11.

Keihm S. J., Tanner, A. and Rosenberger, H. 2004: Measurements and calibration of tropospheric delay at Goldstone from the Cassini media calibration system, *IPN Progress Report* 42-158.

Kliore, A. J., D. L. Cain, 1968, Mariner V and the radius of Venus, *Journal of Atmospheric Science* 25, 549-554.

Kliore, A., D.L. Cain, T.W. Hamilton, 1964: Determination of some physical properties of the atmosphere of Mars from changes in the Doppler signal of a spacecraft on an Earth-occultation trajectory, Technical Report 32-674, Jet Propulsion Laboratory, Pasadena, California.

Kliore, A., D.L. Cain, G.S. Levy, V.R. Eshleman, G. Fjeldbo, and F.D. Drake, 1965: Occultation experiment: results of the first direct measurement of Mars atmosphere and ionosphere, *Science* 149, 1243-1248.

Kliore, A. J., J. D. Anderson, J. W. Armstrong, S. W. Asmar, C. L. Hamilton, N. J. Rappaport, H. D. Wahlquist, R. Ambrosini, B. Bertotti, F. M. Flasar, R. G. French, L. Iess, E. A. Marouf, A. Nagy, 2004: Cassini Radio Science, *Space Science Reviews* 115, 1-70.

Kliore, A. J., A. F. Nagy, E. A. Marouf, R. G. French, F. M. Flasar, N. J. Rappaport, A. Anabtawi, S. W. Asmar, D. S. Kahan, E. Barbinis, G. L. Goltz, D. U. Fleeischman, and D. J. Rochblatt, 2008. First results from the Cassini radio occultations of the Titan ionosphere. *Journal of Geophysical Research: Space Physics* (1978–2012), 113(A9).

Lindal, G.F., 1992: The Atmosphere of Neptune: An Analysis of Radio Occultation Data Acquired With Voyage 2, *Astronomical Journal* 103, 967-982.

Lipa, B. and G.L. Tyler, 1979: Statistical and computational uncertainties in atmospheric profiles from radio occultation: Mariner 10 at Venus, *Icarus* 39, 192-208.

Marouf, E.A., G.L. Tyler, and V.R. Eshleman: 1982: Theory of radio occultation by Saturn's rings, *Icarus* 49, 161-193.

Marouf, E.A., G.L. Tyler, H. A. Zebker, R.A. Simpson, V.R. Eshleman, 1983: Particle size distribution in Saturn's rings from Voyager 1 radio occultation, *Icarus* 54, 189-211.

Marouf, E.A., G.L. Tyler, and P.A. Rosen, 1986: Profiling Saturn's rings by radio occultations, *Icarus* 68, 120-166.

Marouf, E A, Flasar, M, French, R G, Kliore, A J, Nagy, A F, Rappaport, N J, McGhee, C A, Schinder, P J, Simpson, R A, Anabtawi, A, Asmar, S W, Barbinis, E, Fleischman, D U, Goltz, G L, Kahan, D S, Kern, A, Rochblatt, D., 2006, "Evidence for Likely Liquid Hydrocarbons on Titan's Surface from Cassini Radio Science Bistatic Scattering Observations," AGU Fall Meeting 2006, abstract P11A- 07.

Marouf, E., Rappaport, N., French, R., Simpson, R., Kliore, A., McGhee, C., Schinder, P., Anabtawi, A., 2008, "Dielectric Constant of Titan's South Polar Region from Cassini Radio Science Bistatic Scattering Observations," AGU Fall Meeting 2008, abstract #P21A-1319.

Marouf, E.A. and K. K. Wong, 2012: Documentation of a subset of Cassini radio occultation profiles of Saturn's rings to be archived with the NASA PDS by the end of September 2012; see http://pds-rings.seti.org/cassini/rss/index.html

Moyer, T. D., 2003: *Formulation for Observed and Computed Values of Deep Space Network Data Types for Navigation,* Wiley, Hoboken.

Muller, P. M., W. I. Sjogren, 1968: Mascons: Lunar mass concentrations, *Science* 161, 680-684.

Phinney, R. A and D. L. Anderson, 1968: On the occultation method for studying planetary atmospheres, *Journal of Geophysical Research* 73, 5, 1819-1827.

Rosen, P.A. 1989:, *Waves in Saturn's Rings Probed by Radio Occultation*, Ph.D. Dissertation, Stanford University, Stanford, CA, Appendix B.

Schinder, P.J., F. M. Flasar, E. A. Marouf, R. G. French, C. A. McGhee, A. J. Kliore, N. J. Rappaport, E. Barbinis, D. Fleischman, and A. Anabtawi, 2012: The structure of Titan's atmosphere from Cassini radio occultations: Occultations from the Prime and Equinox missions, *Icarus* 221, 1020-1031.

Simpson, R.A., 2007: Planetary Exploration, chapter 5 in Advances in Bistatic Radar, edited by N.J. Willis and H.D. Griffiths, SciTech Publishing Inc., 494 p.

Thorne, K.S., 1987: Gravitational radiation, In 300 Years of Gravitation, eds. S.W. Hawking and W. Israel, Cambridge, Cambridge University Press.

Tortora, P., Iess, L., Bordi, J.J., Ekelund, J.E., Roth, D.C. 2004: Precise Cassini navigation during solar conjunctions through multifrequency plasma calibrations, *Journal of Guidance, Control and Dynamics, 27*, 251-257

Tyler, G. L., 1987: Radio Propagation experiments in the outer solar system with Voyager, *Proceedings of the IEEE* 75,10, 1404-1431.

Tyler, G.L., G.Balmino, D.P. Hinson, W.L. Sjogren, D.E. Smith, R. Woo, S.W. Asmar, M.J. Connally, C.L. Hamilton, R.A. Simpson, 1992: Radio science investigations with Mars Observer, *Journal of Geophysical Research* 97, 7759-7779.

Will, C. M. 2006: The confrontation between general relativity and experiment: a centenary perspective. *Progress of Theoretical Physics Supplement* 163, 146-162.

Yakovlev, O.I., 1985: *Propagation of Radio Waves in Space*, Moscow, USSR, Science (in Russian; English translation available on books.google.com)

Zebker, H.A., E.A. Marouf, G.L. Tyler, 1985: Saturn's rings: particle size distribution for thin layer models, *Icarus* 64, 531-548.

Appendix 1 Cassini Radio Science Activities Spreadsheet

This spreadsheet lists activities carried out by the Cassini Radio Science Team, their times, the operating modes used, and comments. It provides a very terse overview of RSS data collection. As part of the Mission Closeout activities, it will be hosted on NASA's PDS, and this User's Guide will be updated with a URL for the Activities Spreadsheet once it has been posted.

Appendix 2 Cassini Archived Data Set Spreadsheet

This spreadsheet briefly lists the archived data set for the Cassini RSS time. It provides a very terse overview of RSS data collection. As part of the Mission Closeout activities, it will be hosted on NASA's PDS, and this User's Guide will be updated with a URL for the Activities Spreadsheet once it has been posted.